

~~RESTRICTED~~

RM E51G27

NACA RM E51G27

~~N 5-6~~
02
NACA

RESEARCH MEMORANDUM

SECONDARY FLOWS IN ANNULAR CASCADES AND EFFECTS ON
FLOW IN INLET GUIDE VANES

By Seymour Lieblein and Richard H. Ackley

Lewis Flight Propulsion Laboratory
Cleveland, Ohio

CLASSIFICATION CANCELLED

Authority J. W. Crowley Date 12/9/53
J. E. O. 105-010
By M. H. A. 12/24/53 See diagram
R 7 1657

CLASSIFIED DOCUMENT

This document contains classified information affecting the National Defense of the United States within the meaning of the Espionage Act, USC 50:31 and 32. Its transmission or the revelation of its contents in any manner to an unauthorized person is prohibited by law.

Information so classified may be imparted only to persons in the military and naval services of the United States, appropriate civilian officers and employees of the Federal Government who have a legitimate interest therein, and to United States citizens of known loyalty and discretion who of necessity must be informed thereof.

NATIONAL ADVISORY COMMITTEE
FOR AERONAUTICS

WASHINGTON
August 24, 1951

~~RESTRICTED~~

UNCLASSIFIED



UNCLASSIFIED

NATIONAL ADVISORY COMMITTEE FOR AERONAUTICS

RESEARCH MEMORANDUM

SECONDARY FLOWS IN ANNULAR CASCADES AND EFFECTS ON FLOW IN

INLET GUIDE VANES

By Seymour Lieblein and Richard H. Ackley

SUMMARY

An analysis of the flow across an annular cascade of axial-flow inlet guide vanes was conducted in order to evaluate the role of secondary flows in causing discrepancies between design and observed velocity diagrams. A qualitative discussion of the general nature of the secondary flows within the passages of stationary annular cascades with radial design variations of circulation is presented for both the end-wall boundary-layer regions and the central potential-flow regions of the blade passage. Deviations from ideal mean outlet flows (as determined on the basis of blade-element performance) were shown to exist in the potential-flow region of the vanes because of conditions imposed by the end-wall boundaries, the displacement of the wall boundary-layer surfaces, and the irrotationality requirement. As a consequence of the existence of nonuniform radial flows across the blade spacing in the actual flow through cascades, it may not generally be possible to obtain any arbitrarily specified design variation of turning angle along the radial height of a blade row.

Quantitative evaluations of the variation of the actual mean flow leaving a row of inlet guide vanes were obtained by the method of singularities in which a distribution of vorticity directly proportional to the ideal circulation variation of the design was superimposed on the ideal blade-element flow. Induced turning-angle deflections were calculated from the induced velocities of the superimposed vortex system. With the use of an empirically determined correlation factor, good agreement was obtained between calculated and experimental radial variations of turning angle for several conventional inlet guide vanes for which accurate blade-element turning-angle design data were available.

INTRODUCTION

The existence of secondary flows within the passages of blade rows is recognized as having an important effect on the performance of

UNCLASSIFIED

axial-flow compressors and turbines (references 1 and 2). The term "secondary flow" is generally used to represent deviations of the actual flow from distributions determined on the basis of the performance of individual blade elements. Secondary flows in a cascade of blades arise primarily from the effects of blade twist and end-wall boundary layers.

The effects of secondary flows on the performance of a series of blade rows may be classified into two general types: The first effect appears as a direct or inherent loss due to the absorption of energy from the through flow in order to produce the secondary motions and due to the partial dissipation of this energy by viscous action. The second effect is an indirect or matching loss due to the deviations from design values of the direction and magnitude of the velocities leaving one blade row and entering the next. The magnitude of the inherent loss depends on the strength of the secondary flows, as represented by the vorticity of the motions, and upon the degree to which the associated energy is recovered as useful energy. Total-pressure losses arising from secondary flows in a two-dimensional cascade are shown in reference 3; and in references 4 and 5 a considerable portion of the losses in axial-flow compressors at design conditions is attributed to induced drag.

The problem of secondary flows in rectangular curved passages and cascades of airfoils has been investigated on the basis of both airfoil theory (references 3, 6, and 7) and channel theory (references 8 and 9). In the airfoil-theory approach, induced drag and angle deflections are calculated from considerations of the trailing vorticity associated with spanwise variations of circulation (blade loading). References 3 and 6 present analyses of induced effects at the blade midspan on the basis of the assumption that the blade lift falls off in the wall boundary-layer regions and gives rise to a trailing vortex system of the conventional horseshoe form. In reference 7, a continuous solution and a continuous vortex sheet expressed in terms of a Fourier series are treated. All developments are based on rectangular cascade flow, and no experimental verification of the accuracy of calculated induced deflections along the length of the span of a blade is presented.

The airfoil-theory approach, which is based on the concept of the similarity of the trailing vortex systems of isolated and cascade airfoils, can be recognized to contain several disadvantages. The general nature and strength of the trailing vorticity in the blade end regions (wall boundary-layer regions) of cascade airfoils are not definitely known, and there exists some question concerning the validity of the usual relations among blade lift, circulation, and trailing vorticity in the end regions of cascade airfoils. The airfoil approach, in addition, is incapable of presenting a detailed picture of the physical nature of the flow at points within the passage between blades.

2198 Solutions for the flow within blade passages of cascades have been obtained by means of the channel-theory approach. From considerations of the flow in curved channels with large inlet boundary layers, it is shown in references 8 and 9 that secondary circulations will occur in the outlet flow because of a type of gyroscopic effect on the inlet boundary-layer vorticity as the air is turned by the passage. According to the results of these references, this type of secondary flow is restricted to the regions along the blade in which the entering velocity is nonuniform in profile along the span. For cascades with relatively thin wall boundary layers, however, no information concerning the flow in the central region of the cascade where the inlet total pressure is uniform is obtained from this approach.

Cascade configurations containing thin wall boundary layers are frequently found in axial-flow-compressor research and design; the principal examples are the two-dimensional blade-testing tunnels, the inlet guide vanes of multistage units, and the first rotor row of compressors without inlet guide vanes. An investigation of secondary flows in inlet guide vanes reported herein was made at the NACA Lewis laboratory to evaluate, by means of theoretical analysis and experimental correlation, the role played by secondary flows in causing discrepancies between design and observed velocity diagrams, and to present an approximate method of predicting the variation of the actual mean flow along the span of conventional axial-flow inlet guide vanes.

A qualitative discussion of the general nature of the secondary flows within the passages of stationary annular cascades is presented for both the end-wall boundary-layer regions and the central potential-flow regions of the blade passage. From considerations of the conditions imposed by the end-wall or casing boundaries, the spanwise displacement of the wall boundary layers, and the irrotationality requirement, it is shown that secondary flows must exist in the potential-flow regions of the blades. These deviations from the ideal mean through flows (calculated on the basis of blade-element performance) are due primarily to the effects of variations of spanwise velocity across the spacing between blades.

Quantitative evaluations of the variation of the actual mean flow along the span of cascade blades were obtained by the method of singularities, in which a distribution of vorticity related to the blade design was superimposed on the ideal blade-element flow of the cascade to correct for the effects of finite casing boundaries and wall boundary layers. Induced turning-angle deflections were calculated from the induced effects of the superimposed vortex system. Calculations were made for six axial-flow guide vanes in annular cascade. From a comparison of the theoretical and experimental air turning angles, a correlation factor was obtained for the theoretical induced turning angle that resulted in good agreement between the theoretical and experimental turning angles along the span of the blade for all cases.

QUALITATIVE ANALYSIS

The flow at the inlet to axial-flow inlet guide vanes is usually characterized by relatively thin boundary layers at the end walls and a region of substantially constant total pressure over the greater portion of the blade height. For purposes of analysis, therefore, the cascades considered will be divided into two regions: a boundary-layer region at the end walls and a potential-flow region over the remainder of the blade height. Cascades with passages of constant inner and outer radius and with no blade end clearance are assumed.

Boundary-Layer Region

For an appraisal of the secondary circulations existing in the wall boundary regions of cascades of airfoils, recourse is made to the results of references 8 and 9. In these papers, the vorticity parallel to the flow at the outlet of cascades, to a first approximation for parallel inlet flow, is shown to be given by

$$\xi = -2(\Delta\beta) \frac{dV}{dx} \quad (1)$$

where $\Delta\beta$ is the air turning angle and dV/dx is the gradient of the velocity distribution along the span in the inlet boundary layer (inlet vorticity) at the blade ends. (For convenience, all symbols used herein are defined in appendix A.) The secondary circulation associated with this vorticity appears as shown by the streamlines of the secondary flow in figure 1(a), where the circulatory velocity in the center of the region is zero. Although equation (1) was derived for rectangular cascades and included the assumptions of negligible viscous forces (as would be the case with large boundary layers) and fixed total-pressure surfaces as the fluid passes through the cascade, this general type of motion must exist in the case of annular cascades with relatively thin boundary layers and where some distortion of the boundary-layer surfaces occurs. Because of this circulatory flow, a marked variation in the mean turning angle of the fluid would be expected across the boundary layer with an underturning near the free stream and an overturning near the wall. This increase in turning angle at the blade ends has been well established experimentally (references 1 and 3, for example), thus confirming the direction of the secondary flows. A typical example of an experimental turning-angle variation in a two-dimensional cascade is shown in figure 1(b).

In addition to the circulatory flow illustrated in figure 1(a), considerations of the pressure gradients between blade surfaces reveal (references 10 and 11) that a deflection of the through-flow streamlines in the boundary-layer regions will occur toward the wall near the

pressure surface of the blade and away from the wall near the suction surface. As shown in figure 1(c), this distortion of the boundary-layer interface gives rise to a thickening of the boundary layer on the suction surface and a thinning of the boundary layer on the pressure surface.

The deflection of the streamlines in the boundary-layer regions is explained by the following considerations: The centrifugal force arising from the curved motion through the cascade passage creates a difference in pressure from pressure to suction surface that persists across the relatively thin boundary layers to the end walls. The pressure gradient normal to the direction of the streamline ds is very closely given by

$$\frac{dp}{ds} = \rho \frac{V^2}{r_c} \quad (2)$$

where V and r_c are the free-stream velocity and radius of curvature, respectively, in planes parallel to the side walls at the boundary-layer interface (fig. 1(d)). As the velocity is decreased within the boundary layer, the reduced kinetic energy of the flow becomes insufficient to balance the imposed pressure gradient, and a deflection of the flow toward the suction surface results; that is, r_c must be reduced. The streamline deflection is greatest, of course, adjacent to the walls where the velocities are smallest. As a result of this deflection, the turning angle increases as the wall is approached and the boundary-layer flow is displaced toward the blade suction surface. The same result of an increase in turning angle in the boundary layer at the walls was obtained in reference 12, from an analysis of turbulent boundary layers in three-dimensional flow.

The displacement phenomenon in annular cascades is probably somewhat more complex than in rectangular cascades because of the additional effects of radial displacement of the main body of fluid due to radial pressure equilibrium requirements, and of possible radial displacement of the boundary layers on the blade surfaces toward the hub due to the radial centrifugal force field. Experimental evidence of the wall boundary-layer displacement toward the blade suction surfaces is given in references 3 and 13; typical examples are shown in figures 1(e) and 1(f) of this report. The principal general effects of the secondary flow in the wall boundary-layer regions are thus tendencies toward underturning near the free-stream side and overturning near the end walls, and a thickening of the wall boundary layers toward the suction surfaces.

Potential-Flow Region

Over the main portion of the cascade channel, the inlet vorticity is zero (constant total pressure and temperature) and therefore no complete circulatory motions occur in the outlet flow in this region; that is, the fluid remains irrotational. Mathematically, for flow in an annular passage, the irrotationality condition requires that in a plane normal to the axis,

$$\frac{\partial(rv_{\theta})}{\partial r} = \frac{\partial v_r}{\partial \theta} \quad (3)$$

Although equation (3), strictly speaking, applies locally to a point in the fluid, the relation is used to obtain an estimate of the mean flow between blades by considering equation (3) to represent circumferentially averaged conditions. Thus on the average, for any radial variation of whirl rv_{θ} , a specific variation in radial velocity must exist across the spacing from blade surface to blade surface.

Free-vortex blading. - For the case of perfect compressible flow across a free-vortex cascade (without wall boundary layers), radial pressure equilibrium requires that a radial displacement of the flow occur toward the tip across the blade row. Thus within the passage between blades, radial components of velocity outward toward the tip casing generally exist. At the same time, boundary conditions require that the radial velocity at the walls at hub and tip be zero. It is possible, however, for the radial velocity to vary along the radius with constant magnitudes across the spacing and thus meet the irrotationality requirement for this type of blading that the tangential gradient of V_r be zero at all points, as shown in figures 2(a) and 2(b). Constant circulation along the radius may therefore be obtained from free-vortex blading in the absence of wall boundary layers. Radial velocity outward toward the tip and tangential velocity from pressure surface to suction surface are considered positive.

In an actual fluid where end-wall boundary layers are present, however, the displacement of the boundary layer toward the blade suction surface results in opposite radial displacements of the main body of the fluid over the pressure and suction surfaces of the blade. As illustrated in the exaggerated plan view of figure 3(a) for the case of equal average boundary-layer thickness at inlet and outlet, the radial motion is outward toward the walls at the pressure surface and inward away from the walls at the suction surface (see photographs in reference 1). For cascades in which the average boundary-layer thickness at the outlet is greater than that at the inlet, the radial deflections introduced by the wall boundary layers will be more pronounced over the suction surface of the blades, as illustrated in figure 3(b).

In any particular cascade, the resultant radial motion at points within the blade passages is the combination of the radial flows due to the wall boundary-layer displacement, the prevailing radial flows arising from the requirements of radial pressure equilibrium, and the possible radial motions of the blade surface boundary layers.

Because of the radial motion introduced by the wall boundary layers, V_r is not constant across the spacing as shown in figure 4(a), and as a consequence the whirl rV_θ cannot remain constant along the radius. With the tangential gradient of V_r positive on the left side of the channel and negative on the right, rV_θ must decrease from the midspan of the passage to the boundary layers (fig. 4(b)). The blade circulation and air turning angle, being functions of the outlet whirl, will likewise tend to decrease from the center of the passage to the boundary layers compared with the variations for perfect blade-element flow. The complete variation of mean air turning angle along the radial height of a free-vortex cascade appears as shown in figure 4(c). Figures 4(d) and 4(e) illustrate the radial velocity and whirl components for a decelerating cascade. A similar radial variation of turning angle is to be expected for staggered cascades. A typical example of an experimental radial variation of air turning angle across a conventional free-vortex turbine-inlet nozzle obtained from reference 20 is illustrated in figure 4(f).

In general, the deviations of the actual flow from the ideal blade-element flow in free-vortex cascades with wall boundary layers can be obtained from the superposition of the ideal through flow and an apparent secondary flow of the type shown in figure 4(g). The secondary velocities are strongest along the boundary-layer interface and adjacent to the walls, and a complete circulatory streamline path of the secondary flows exists only in the boundary-layer regions.

Variable-circulation blading without wall boundary layers. - In many cases, inlet guide vanes are designed to produce outlet rotations involving a variation of circulation along the radius (such as constant turning, constant tangential velocity, or wheel-type diagrams). For such designs, according to equation (3), the radial velocity is no longer constant across the spacing and the compatibility of prescribed circulation variations and corresponding radial velocities must be investigated. As an illustration of the secondary flows arising in this type of blading, a qualitative analysis of the flow across a cascade designed for radially constant outlet tangential velocity will be made.

For a cascade with constant tangential velocity along the radius, from equation (3), on the average

$$\frac{\partial(rv_{\theta})}{\partial r} = \frac{\partial v_r}{\partial \theta} = \text{constant} \quad (4)$$

and the radial velocity must vary approximately linearly across the spacing. Inasmuch as the whirl increases with radius, the absolute magnitude of the radial velocity (which is negative) on the pressure surface will be greater than on the suction surface, and the required variation of radial velocity will appear as in figure 5(a). The mean radial displacement is toward the hub for this type of blading. Consider the case of no wall boundary layers: Along the inner and outer walls,

$$v_r = 0$$

and

$$\partial v_r / \partial \theta = 0$$

Furthermore, inasmuch as the radial velocity must vary continuously throughout the flow passage between blades, some radial distance is required before the radial velocity can attain its required tangential variation. There exists, therefore, a region near the walls in which the circumferential variation of v_r is less than the value required for a linear increase in rv_{θ} (fig. 5(b)). In the blade end regions, therefore, the required circulation gradient cannot be maintained and the gradients will approach zero values at the walls, as illustrated in figure 5(c). In any particular cascade, the magnitude of the deviation of the actual circulation will depend upon many factors, such as the geometry of the cascade (blade shape, solidity, aspect ratio, and so forth) and the blade loading. A three-dimensional analysis of the flow through cascade passages may be required for a complete point-to-point solution across the passage.

The radial variation of air turning angle across the cascade is generally similar in form to the circulation variation, and, therefore, an underturning in the tip region and an overturning in the hub region of the blades would be expected (fig. 5(c)). This type of turning-angle deviation applies generally to all forms of radially increasing design circulation gradients, where the exact form and magnitude of the deviations depend upon the cascade and the form and magnitude of the design circulation gradient. Similarly, if a radially decreasing variation of circulation were prescribed, an overturning in the tip region and an underturning in the hub region would result, as shown in figure 5(d). Thus, as a consequence of the effects of the boundary conditions imposed by the end walls, it is not generally possible to achieve any arbitrary design variation of turning angle along the span of cascade blades, even in the absence of wall boundary layers. In all cases, the trend of the actual turning-angle variation is in the

direction of a decrease in the magnitudes of the turning-angle gradients in the end regions of the blades.

Variable circulation blading with wall boundary layers. - When boundary layers are present along the end walls of cascades with variable circulation blading, radial motions in addition to those arising from the requirements of radial pressure equilibrium are superimposed on the main body of the flow. These additional radial motions arise from the distortion of the boundary-layer interface as the fluid passes through the cascade. As previously indicated, these radial displacements are relatively outward toward the walls near the pressure surface and inward away from the walls near the suction surface. The additional radial flows introduced by the wall boundary-layer displacement are shown in figure 6(a) for the illustrative cascade with radially increasing design circulation. Near the tip region of the blade, the radial velocities imposed by the boundary-layer distortion will tend to decrease the gradient of the radial velocity across the passage (fig. 6(b)). According to equation (3), therefore, a smaller radial gradient of whirl can be maintained in this region, and a further reduction in circulation and turning angle will result. In some cases, if the boundary-layer displacement is pronounced and the radial circulation gradient is small, the sign of $\partial V_r / \partial \theta$ may be reversed and the circulation may actually decrease as the boundary layer is approached (as, for example, the limiting case of free-vortex flow, fig. 4(f)).

In the hub region of the blade, the radial velocities associated with the boundary-layer displacement tend to increase the value of $\partial V_r / \partial \theta$ across the spacing (fig. 6(c)) and permit a larger radial variation of whirl to be maintained. The turning angles in the hub region will therefore decrease compared with the magnitudes without wall boundary layers in the direction of the original design variation. The complete radial variation of turning angle in a cascade with wall boundary layers and radially increasing design circulation would therefore appear as shown in figure 6(d). For radially decreasing circulation, the reverse trend would occur in the potential-flow region.

In an actual cascade, the real flow is considerably more complex than the somewhat simplified concept of the flow given here. For example, the existence of flow separation, shocks, blade-end clearance with leakage flows, or radial displacements of the boundary layers along the blade surfaces may impose further radial motions on the main flow that will to some extent alter the qualitative results obtained in the preceding analyses. Although the existence of a tapering of the annulus passage in the axial direction will increase the magnitude of the mean radial motions, the blade-to-blade gradients of V_r and the general secondary-flow picture will not be materially affected by conventional hub or shroud tapers. For conventional unstalled subsonic inlet guide vanes with small end clearances, the secondary-flow effects as presented herein should predominate.

In figure 7 are presented examples of the experimental variation of air-turning angle along the radius of typical inlet guide vanes designed for both radially increasing and radially decreasing circulation. For the vane with radially decreasing circulation, the turning angles in the tip region are very small and therefore the tip boundary-layer displacement is likewise small. The measured turning-angle variation in this region thus approaches the trend anticipated for the case of a cascade without wall boundary layer (fig. 5(d)).

Trailing Vorticity

In the preceding sections, secondary flows were shown to exist within the passages of annular cascades when variations of radial velocity exist across the blade spacing. When the flow leaves the blade passages, these unequal radial velocities on the blade pressure and suction surfaces form surfaces of discontinuity or shear surfaces in the wakes; this formation corresponds to the formation of a sheet of trailing vortices. The strength of the trailing vorticity at any radial position depends on the magnitude of the radial velocity difference across the blade wake at the trailing edge. The qualitative variations of trailing vorticity along the radial height of a cascade are estimated to appear as shown in figure 8 for the various types of blading considered. Counter-clockwise rotation is taken as positive vorticity. In all cases, because of the vanishing of the radial velocities at the walls, the trailing vorticity at the walls is zero. The potential induced losses will exhibit corresponding variations (proportional to absolute magnitude of ξ), and will generally be greatest near the hub region for blades with radially increasing design circulations and near the tip region for blades with radially decreasing design circulations.

The boundary requirement of zero trailing vorticity and nonzero values of lift (as determined by surface pressure distributions) at the ends of cascade blades, constitutes a significant difference between the end flows of isolated and cascade airfoils. The assumption of the complete reduction of lift in the boundary-layer regions and the subsequent formation of trailing vorticity based on this lift gradient (as in references 3 and 6) is therefore not representative of the actual flow in cascades. For example, according to the concepts of references 3 and 6, the trailing vorticity in the boundary-layer region attains its maximum magnitudes as the casing wall is approached, whereas the true trailing vorticity tends to vanish. It is also apparent that the usual relations among lift, circulation, and trailing vorticity are no longer valid in the end regions of cascade blades when wall boundary layers are present.

QUANTITATIVE ANALYSIS

Method of Singularities

2198 The problem of obtaining quantitative methods of evaluation of the secondary flows in cascades appears quite complex because of the three-dimensional nature of the phenomenon in both the potential-flow and wall boundary-layer regions. As an approach to the problem, references 3, 6, and 7 make use of the method of singularities in which a trailing vortex field (normally associated with the flow about isolated airfoils) was employed to calculate the induced downwash behind the cascade. This method contains an apparent anomaly, however, in that the direction of the induced velocities must be reversed in order to obtain the correct change in circulation and turning angle compared with the two-dimensional or blade-element values.

The approach of this report presumes that actual radial variations of air turning angle at the outlet of annular cascades can be satisfactorily approximated by applying corrections to the ideal turning-angle variation as determined from considerations of the performance of individual blade elements. The method involves the superposition on the ideal flow of a vortex system parallel to the flow in the plane of the blades to correct for the effects of the casing boundaries and the wall boundary layers.

Because of the approximate nature of the method, for simplicity the entire outlet flow is assumed to leave the blade row axially and the cascade blades are assumed to be replaceable by lifting lines of variable strength, as indicated in figure 9(a). Corrections to the ideal mean (circumferentially averaged) blade-element flow are obtained from consideration of the induced velocities associated with the superimposed vorticity and are calculated in the plane of the blades. It is also presupposed that empirical correction factors will be necessary to correlate calculated and experimental results satisfactorily.

Flow without wall boundary layer. - The method is demonstrated by considering the illustrative case of blading designed to produce a linearly increasing circulation along the radius. At first, ideal flow across a finite number of blades in an annulus of zero inner radius and infinite outer radius is considered. For the case of radially increasing circulation, a constant circumferential difference in radial velocity is obtained over the blade surface as shown in figure 9(b). The vorticity corresponding to this ideal radial-velocity difference is designated the ideal infinite-flow vorticity of the blade. When the blading is confined between finite annular boundaries, however, the radial velocities at the boundaries must vanish. As previously indicated, as a consequence of the vanishing of the radial velocities at the walls, the trailing vorticity at the boundaries vanishes

(fig. 8(b)); and in the absence of wall boundary layers, an overturning in the hub region and an underturning in the tip region occur (fig. 5(c)).

The satisfaction of the given conditions can be accomplished, to a first approximation, by superimposing a distribution of vorticity on the ideal infinite-flow vorticity of the blade between the casing boundaries. A first type of superimposed vortex distribution might attempt to duplicate the true trailing vorticity of the cascade, as shown in figure 9(c). The superimposed vorticity is equal in magnitude but opposite in rotation to the ideal infinite-flow vorticity of figure 9(b) at the walls and rapidly decreases in strength away from the walls. The net vorticity will then appear as in figure 8(b). As shown in figure 9(c), the induced velocities associated with the superimposed vortex distribution will tend to produce an overturning in the hub region and an underturning in the tip region.

A superimposed vortex distribution of the type shown in figure 9(c) will be very difficult to establish quantitatively as a general procedure because of the absence of a usable relation between the particular blade design and the vortex distribution. An alternate vortex distribution achieving the equivalent induced effects can be obtained, however, by relating the superimposed vorticity directly to the ideal (blade-element) circulation distribution along the entire radius; that is, by employing a vortex distribution equal in strength but opposite in rotational direction to the ideal infinite-flow vorticity at all points along the radius. The vortex system and its induced velocities are shown in figure 9(d) for the illustrative case of linearly increasing circulation. Thus, in a similar manner, the superimposed vortex system can be readily determined for any type of design velocity diagram and corresponding induced velocities can be calculated.

Flow with wall boundary layers. - It was previously shown that when wall boundary layers are present, a reduction in turning angle from midspan to the wall boundary layers and an increase in turning angle across the boundary layer toward the walls occur with respect to the ideal turning-angle variation. This secondary-flow effect can be approximated from the induced velocities of a circular vortex located in each boundary-layer region, as shown in figure 9(e). The diameter of the core of the circular vortex is roughly of the order of magnitude of the thickness of the boundary layer. Inasmuch as the boundary-layer secondary-flow effect was indicated to be a function of the turning angle at the boundary-layer interface, for simplicity the strength of the superimposed boundary-layer vortex cores is taken to be proportional to the magnitude of the circulation at the boundary-layer interface. Thus, the complete superimposed vortex system for the annulus channel is obtained from the addition of the vortices in figures 9(d) and 9(e), where as shown in figure 9(f) for an arbitrary radial variation of circulation of slope $d\Gamma/dr$ (counterclockwise rotation taken as positive),

$$\xi_h \approx \Gamma_h$$

$$\xi \approx \frac{d\Gamma}{dr} dr$$

$$\xi_t \approx -\Gamma_t$$

The corresponding trend of variation of the turning angles as obtained from the induced velocities of the superimposed vortex system is illustrated in figure 9(g) for the case of radially increasing circulation.

In order to completely satisfy the boundary conditions along the inner and outer walls of the annulus, a system of vortex images must be established outside these walls so that the component of induced velocity normal to the wall along the entire surfaces is reduced to zero. For any line vortex at radius r on one side of a circular boundary of radius r_w , the induced velocity normal to the surface of the boundary will be zero if a vortex mirror image of equal strength and opposite rotation is imagined to exist on the opposite side of the wall at a distance r_w^2/r (reference 14). For an annular passage, a cyclic image system results with an infinite number of images extending out toward infinity outside the annulus, and an infinite number of images bunching up toward the center on the inside of the annulus (reference 15). A partial view of the annulus and image vortex system for a guide-vane cascade as seen looking upstream from a point behind the vane is shown in figure 10. The boundary-layer circular vortices are indicated by the larger arcs and the main-span vortex sheets are indicated by the smaller arcs.

Induced Turning Angle

Basic equations. - The total induced velocity at a point along the vane lifting line depends upon the contributions of the two types of trailing vortex that have been established; namely, the boundary-layer circular vortices and the main-span vortex sheet. The velocity induced outside the core at a semi-infinite circular vortex at radius r (fig. 11) at a point located at radius r_p in an annular cascade is given by (reference 16)

$$q = \frac{\Gamma}{4\pi h} \quad (5)$$

and the component normal to the plane of the vane is

$$q_n = \frac{\Gamma}{4\pi h} \sin \psi \frac{r}{h} \quad (6)$$

or, for induced velocities directed downward in figure 11 (in the direction of turning) as positive values,

$$q_n = - \frac{\Gamma}{4\pi} \frac{r_p - r \cos \epsilon}{r^2 - (2r)r_p \cos \epsilon + r_p^2} \quad (7)$$

where ϵ is the angle between the plane of the vane containing the vortex and the plane of the vane containing the point investigated. Equation (7) is valid, to a first approximation, to compressible as well as incompressible flow (reference 17). For the vortex sheet, between the boundary-layer limits

$$q_n = - \frac{1}{4\pi} \int_{r_h + \delta_h}^{r_t - \delta_t} \frac{\frac{d\Gamma}{dr} (r_p - r \cos \epsilon) dr}{r^2 - (2r)r_p \cos \epsilon + r_p^2} \quad (8)$$

At a given point P along the span of a cascade vane (fig. 11), the total normal induced velocity is obtained by summing up the contributions of all the annulus and image line and sheet vortices in the plane of a vane for all vanes in the cascade. Because of the approximate nature of the development, correction factors will be necessary for experimental correlation, so that, in general,

$$q_n = - \frac{C_1}{4\pi} \sum_{j=0}^{N-1} \sum_{k=-\infty}^{+\infty} \left[\frac{\Gamma_h \left[r_p - d_{h,k} \cos \left(j \frac{2\pi}{N} \right) \right]}{r_p^2 - 2d_{h,k} r_p \cos \left(j \frac{2\pi}{N} \right) + d_{h,k}^2} + \frac{\Gamma_t \left[r_p - d_{t,k} \cos \left(j \frac{2\pi}{N} \right) \right]}{r_p^2 - 2d_{t,k} r_p \cos \left(j \frac{2\pi}{N} \right) + d_{t,k}^2} \right] - \frac{C_2}{4\pi} \sum_{j=0}^{N-1} \sum_{k=-\infty}^{+\infty} \int_{(r_h + \delta_h)_k}^{(r_t - \delta_t)_k} \frac{\left(\frac{d\Gamma}{dr} \right) \left[r_p - r_k \cos \left(j \frac{2\pi}{N} \right) \right] dr_k}{r_p^2 - 2r_p r_k \cos \left(j \frac{2\pi}{N} \right) + r_k^2} \quad (9)$$

where

C_1, C_2 arbitrary correction factors

$-k$ represents k^{th} vortex image in inner wall

$+k$ represents k^{th} vortex image in outer wall

j integer

N number of vanes in cascade

The vortices of the vanes within the annulus are designated by $k=0$ and the vane containing the point P , called the primary vane, is characterized by $j=0$.

Inasmuch as vanes equally spaced about the primary vane will contribute equally to the induced velocity at P , equation (9) can be expressed as

$$q_n = \sum_{k=-\infty}^{\infty} (q_n)_{k,j=0} + 2 \sum_{j=1}^{\frac{N-1}{2}} \sum_{k=-\infty}^{\infty} (q_n)_{k,j} \quad (10a)$$

for an odd number of vanes, and for an even number of vanes,

$$q_n = \sum_{k=-\infty}^{\infty} \left[(q_n)_{k,j=0} + (q_n)_{k,j=\frac{N}{2}} \right] + 2 \sum_{j=1}^{\frac{N-2}{2}} \sum_{k=-\infty}^{\infty} (q_n)_{k,j} \quad (10b)$$

The induced turning angle is then obtained (fig. 11) from

$$\Delta\beta_1 = \tan^{-1} \frac{q_n}{V_2} \quad (11)$$

where V_2 is the ideal cascade outlet velocity determined from the blade-element turning angles. For simplicity, equal correction factors for the vortex cores and vortex sheet are assumed; furthermore, the single correction factor now called the correlation factor is applied directly to the turning angle so that

$$\Delta\beta_1 = C \tan^{-1} \frac{q_n}{V_2} \quad (12)$$

where q_n is determined from equation (9) for $C_1 = C_2 = 1$.

Approximate solution. - An exact solution of equation (9) or (10) for an arbitrary variation of circulation along the main span would be extremely complex and lengthy. In view of the simplified nature of the vortex system and the consideration that the induced velocity at a point is affected principally by the vortex system of the primary vane and the vortices close by, an approximate and relatively simple solution of equation (9) was obtained by considering only the image vortices immediately adjacent to the annulus walls and only a few vanes on both sides of the primary vane. This procedure is equivalent to the mathematical condition that a series of the form of equation (9) converges rapidly. In reference 15, a similar type of induced velocity summation is found to be rapidly convergent. The reduced vortex system used in the solution was taken to consist of: (1) the two boundary-layer vortex cores and the main-span vortex sheet of the annulus vanes, and (2) the first hub and tip image vortex cores (located at r_h^2/d_h and r_t^2/d_t , respectively). The upper value of j in equation (10) was arbitrarily set at 3, giving the inclusion of the effect of seven vanes. The error involved in neglecting the remainder of the vortices, whose contribution rapidly diminishes as the distance from P is increased, will be assumed to be absorbed by the empirical correlation factor. From equation (9), therefore, with the correction factors equal to 1,

$$q_n = -\frac{1}{4\pi} \sum_{j=0}^{\pm 3} \left\{ \Gamma_h \left[\frac{r_p - d_h \cos \left(\frac{2\pi j}{N} \right)}{r_p^2 - 2d_h r_p \cos \left(\frac{2\pi j}{N} \right) + d_h^2} - \frac{r_p - \left(\frac{r_h^2}{d_h} \right) \cos \left(\frac{2\pi j}{N} \right)}{r_p^2 - 2 \left(\frac{r_h^2}{d_h} \right) r_p \cos \left(\frac{2\pi j}{N} \right) + \left(\frac{r_h^2}{d_h} \right)^2} \right] + \right. \\ \left. \Gamma_t \left[\frac{r_p - d_t \cos \left(\frac{2\pi j}{N} \right)}{r_p^2 - 2d_t r_p \cos \left(\frac{2\pi j}{N} \right) + d_t^2} - \frac{r_p - \left(\frac{r_t^2}{d_t} \right) \cos \left(\frac{2\pi j}{N} \right)}{r_p^2 - 2 \left(\frac{r_t^2}{d_t} \right) r_p \cos \left(\frac{2\pi j}{N} \right) + \left(\frac{r_t^2}{d_t} \right)^2} \right] + \right. \\ \left. \int_{r_h + \delta_h}^{r_t - \delta_t} \frac{\left(\frac{d\Gamma}{dr} \right) \left[r_p - r \cos \left(\frac{2\pi j}{N} \right) \right]}{r_p^2 - 2r_p r \cos \left(\frac{2\pi j}{N} \right) + r^2} dr \right\} \quad (13)$$

Inasmuch as the main-span circulation variation is determined from design flow conditions in evaluating the integral term of equation (13), it was assumed that the variation of circulation along the radial height of the vane can be represented by a parabolic relation, such that

$$\Gamma = \frac{a}{2} r^2 + br + c \quad (14)$$

and

$$\frac{d\Gamma}{dr} = ar + b \quad (15)$$

Substituting equation (15) in equation (13) and integrating yield, with $\cos \frac{2\pi j}{N} = f$,

$$q_n = -\frac{1}{4\pi} \sum_{j=0}^{\pm 3} \left\{ \bar{\Gamma}_h \left[\frac{r_p - fd_h}{r_p^2 - 2fd_h r_p + d_h^2} - \frac{r_p - f \left(\frac{r_h^2}{d_h} \right)}{r_p^2 - 2f \left(\frac{r_h^2}{d_h} \right) r_p + \left(\frac{r_h^2}{d_h} \right)^2} \right] + \right. \\ \left. \bar{\Gamma}_t \left[\frac{r_p - fd_t}{r_p^2 - 2fd_t r_p + d_t^2} - \frac{r_p - f \left(\frac{r_t^2}{d_t} \right)}{r_p^2 - 2f \left(\frac{r_t^2}{d_t} \right) r_p + \left(\frac{r_t^2}{d_t} \right)^2} \right] - \right. \\ \left. af \left[(r_t - \delta_t) - (r_h + \delta_h) \right] - \frac{1}{2} \left[f(2far_p + b) - ar_p \right] \ln \frac{(r_t - \delta_t)^2 - 2r_p f(r_t - \delta_t) + r_p^2}{(r_h + \delta_h)^2 - 2r_p f(r_h + \delta_h) + r_p^2} + \right. \\ \left. (2far_p + b) \sqrt{1-f^2} \left[\tan^{-1} \frac{\frac{1}{r_p} (r_t - \delta_t) - f}{\sqrt{1-f^2}} - \tan^{-1} \frac{\frac{1}{r_p} (r_h + \delta_h) - f}{\sqrt{1-f^2}} \right] \right\} \quad (16)$$

$r_h + \delta_h = .389$
 $r_p = .39$

where again,

$$q_n = (q_n)_{j=0} + 2 \sum_{j=1}^3 (q_n)_j \quad (17)$$

Inasmuch as the wall boundary-layer thickness generally varies from blade inlet to outlet, the boundary-layer thickness used in the calculation was obtained from both inlet and outlet values as

$$\delta = \delta_2 - \frac{1}{3} (\delta_2 - \delta_1) \quad (18)$$

The distance from the wall to the axis of the boundary-layer vortex cores was set as

$$e = \frac{1}{3} \delta \quad (19)$$

so that the radii at the axis of the vortex cores were

$$d_h = r_h + \frac{1}{3} \delta_h \quad (20a)$$

and

$$d_t = r_t - \frac{1}{3} \delta_t \quad (20b)$$

For a given inlet-guide-vane cascade with the radial variation of circulation approximated by a parabolic equation and the hub and tip boundary layers known or prescribed, all quantities in equations (16) and (17) are determined. Thus, the normal induced velocity at points along the radial height of the vane can be calculated by means of simple numerical computations. The actual turning angle is then obtained from

$$\Delta\beta = \Delta\beta_e + \Delta\beta_i \quad (21)$$

where $\Delta\beta_e$ is the blade-element turning angle at each vane section.

NUMERICAL EXAMPLES

Vane Designs

The induced velocity analysis was conducted for two types of axial-flow-compressor inlet-guide vane: (1) vanes with NACA 65-series camber lines and with constant chord and hub radius, and (2) vanes with circular-arc camber lines and with varying chord length and hub radius across the vanes. Calculations were also made for a turbine-inlet nozzle. Examples involving these three vane configurations were chosen because of the availability of design turning-angle data (references 18, 19, and 20, respectively). Detailed identification data for the various

vane designs investigated are presented in table I. Vanes A and B were designed for supersonic-compressor application and vanes C, D, and E, for conventional subsonic-compressor designs.

Experimental turning-angle data for the compressor-inlet guide vanes were obtained for the most part from unreported investigations. The compressor guide vanes were investigated as separate components in induction-type annular cascades of constant outer diameter and with bellmouth inlet. The turbine-nozzle turning-angle data were obtained from blades mounted in a sector of an annular cascade as reported in reference 20. The axial distance from the inlet face of the bellmouth and the nose of the inlet hub section to the guide-vane leading edge varied from approximately 14 to 20 inches for all vanes.

The investigations were conducted with ambient inlet air; the flow at the inlet vanes was substantially uniform and axial in all cases, and the angle of the air leaving the blade row was taken as the air turning angle. Outlet-air angles were measured by claw-type instruments for designs A through E and by a pitot-type instrument for design F, and were circumferentially averaged at each radial position. Absolute accuracy of the measured angle is estimated to be $\pm 3/4^\circ$ and the relative accuracy from point to point is believed to be within $\pm 1/4^\circ$.

Calculations

General procedure. - The calculation of the induced and actual turning angles for a given guide-vane cascade was based upon the determination of blade-element flow conditions. Blade-element flow conditions were obtained from consideration of the cascade vane as a series of individual elements, and represented the variation of velocity and circulation along the radial height of the vane corresponding to the blade-element turning angles. The blade-element turning angles used in the analysis depended on the nature of the available design data relating the air turning angle with the geometric characteristics of the particular type of guide vane investigated. For a given blade profile, in most cases the available design data had to be corrected to take into account the differences between the cascade configuration and flow conditions of the vane row investigated, and the cascade configuration and flow conditions of the vanes from which the original design data were obtained. The element turning-angle corrections consisted principally of angle adjustments for differences in inlet Mach number (compressibility) and radial displacement of the flow due to hub taper.

The principal steps involved in the determination of the actual mean flow across inlet guide vanes were therefore associated with the calculation of the following quantities:

- (1) Corrected blade-element turning angle
- (2) Blade-element circulation and outlet velocity
- (3) Induced velocity and turning angle (from equations (12), (16), and (17))
- (4) Actual turning angle (from equation (21))

Details of the element corrections to the design data are given in the sections for the different types of vane considered. Equations for the calculation of outlet velocity and circulation for a given radial variation of turning angle are presented in appendix B.

The annulus boundary-layer thicknesses at hub and tip were determined from experimental total-pressure distributions whenever available. In cases where experimental boundary-layer data were unavailable, the average thickness at both hub and tip was taken as 0.06 of the blade height for the designs with low hub-tip ratio (0.5 to 0.6) and as 0.08 of the blade height for the designs with high hub-tip ratio (0.7 to 0.8). These approximate ratio values were obtained from previous surveys of the performance of conventional bellmouth inlet sections.

From the calculated variation of blade-element circulation and the average boundary-layer thicknesses, the magnitudes of the circulations at the limits of the boundary layers (Γ_t and Γ_h) were determined (fig. 9(f)). The determination of the constants a and b for the best parabolic curve representing the blade-element circulation then completed the quantities required for the calculation of the induced velocity (equations (16) and (17)).

Vanes with NACA 65-series camber lines. - Design turning-angle data for inlet guide vanes with NACA 65-series mean lines were obtained from reference 18. The design data were obtained for essentially incompressible flow, and inasmuch as the design inlet Mach number of the subject vanes was 0.6, a compressibility correction to the original design data was necessary. The compressibility correction was made according to the method of reference 21. Inasmuch as the design data of reference 18 were obtained for conditions of essentially incompressible flow and constant axial velocity across the cascade, equation (13) of reference 21 was used for the compressibility correction. Values of axial-velocity ratio $V_{z,1}/V_{z,2}$ along the vane height at the given inlet Mach number were calculated according to the method of appendix B using the design turning angles.

Vanes with circular-arc camber lines. - Design turning-angle data for the constant-thickness circular-arc guide vanes were obtained from reference 19. Inasmuch as the vanes investigated were set in convergent passages, the straight-line rule for convergent annuli of reference 19 was used for the design data. The blade-element corrections for hub taper and variable chord length applied to the design rule are discussed in detail in appendix C.

Turbine nozzle. - The blade-element turning-angle variation for the turbine nozzle was taken directly from the design outlet angles as given in reference 20.

Examples. - The various turning angles calculated when determining the mean actual turning angle of inlet guide vanes (steps 1 to 4) are illustrated in figure 12, with vanes B and D as examples. The induced turning angles were calculated at six radial positions r_p along the height of the vanes between the boundary layers; at points 0.13 to 0.15 inch from the limits of the boundary layers, and at points measured from the vane mean radius at locations approximately 0.45 and 0.85 of the distance between the mean radius and the outermost r_p locations. Induced turning angles at r_p stations closer than approximately 0.13 inch from the boundary layers were not believed to be realistic values because of the tendency of the calculated induced velocities, as given by equations (16) and (17), to approach infinite magnitudes at the boundary-layer limit. The actual turning angles in the boundary-layer regions were therefore extrapolated to indicate the trend of the variation as determined from considerations of the secondary flows and the directions of the induced velocities in the boundary-layer regions. Theoretical induced turning angles in the boundary-layer regions were calculated for vane F at the axes of the circular vortices in order to substantiate the qualitative trends.

RESULTS AND DISCUSSION

Experimental correlation. - Theoretical values of induced turning angle without a correction factor were first calculated for the various guide vanes investigated. From a comparison of calculated and experimental radial variations of mean turning angle, it was found that good agreement between calculated and observed results could be obtained with the use of a constant correlation factor of 0.42. The calculated variations of actual turning angle along the radial height of the vane for the six guide-vane designs investigated are shown in comparison with observed values in figure 13 for this correction factor. The original design data turning angles and induced turning angles are also shown in figure 13.

An example of the radial variations of theoretical axial and tangential velocity resulting from the calculated actual turning angles for vane C is shown in comparison with design and experimental values in figure 14. The axial and tangential velocities for the design and actual cases were calculated according to the method of appendix B for the same flow-area contraction and polytropic efficiency. Design and theoretical total velocities were practically the same.

With the use of the empirically determined correlation constant, the induced velocity analysis presented herein can be used with good accuracy as a method of calculating the actual mean flow across similar inlet guide vanes when reliable turning-angle design data (two-dimensional cascades and so forth) are available. In all examples, however, the radial variation of design axial velocity from hub to tip was relatively small (no greater than 17 percent). The method as presented therefore may not necessarily produce results of equivalent accuracy for cases of large design axial-velocity gradients without suitable modification of the blade-element turning angles.

Rotor-inlet conditions. - The theoretical effect of guide-vane secondary deflections on the inlet flow relative to a succeeding row at design tip speed was investigated for vanes C and E. Air inlet angles and velocities relative to the rotor were calculated on the basis of guide-vane design data and actual turning angles are shown in comparison with experimental values in figure 15. Despite the large secondary deflections in the guide-vane outlet flow, the design and calculated relative inlet angles are very similar in both trend and magnitude. At high values of design relative inlet angle, if little change occurs in the magnitude of the absolute inlet velocity, changes in guide-vane outlet angle result in very small changes in rotor relative inlet angle. As can be seen from considerations of rotor velocity diagrams, rotor relative inlet angles (and consequently rotor-blade angle of attack) become more sensitive to guide-vane induced deflections as the magnitudes of the design relative inlet angles are reduced. For example, for vane E, if the rotor inlet angle is reduced from 65° to 50° (by reducing the wheel speed), the maximum difference between the relative inlet angle as calculated from design turning data and the relative inlet angle as obtained from calculated actual turning angles increases from a value of somewhat less than 1° to a value of 2° . The corresponding maximum difference for vane C was increased to $2\frac{1}{2}^\circ$ at an average relative inlet angle of 27° . For relative inlet angles near 0° , the magnitudes of the rotor induced inlet-angle deflection approach those of the guide vane induced outlet-angle deflections.

The principal effect of the theoretical guide vane secondary flows on rotor-inlet conditions at design rotor speeds appears, as shown in figure 14, as a change in the magnitudes of the design inlet velocities.

For large guide-vane induced deflections, these velocity changes may cause significant variations in rotor-inlet Mach number and therefore energy transfer and diffusion. In addition, the existence of trailing vorticity shed downstream of the guide vanes when secondary flows occur may have a significant effect on the flow distributions through the rotor. Rotor-entrance conditions cannot be considered irrotational.

Correlation factor. - The induced-deflection correction factor of 0.42 found necessary to correlate satisfactorily the absolute magnitudes of calculated and observed turning angles of the various guide vanes tested indicates an apparently large degree of error in the representation of the true secondary flows by means of a superimposed correction vortex system. Although the simplification of the cascade configuration, the partial summations, and the location of the boundary-layer line vortices have some influence on the magnitude of the calculated induced velocities (fig. 16, for example), the excessive induced deflections obtained from the calculation are due primarily to the unknown proportionality relation between the true vorticity in the boundary-layer regions and the vorticity assumed by the method. In the potential-flow region of the vanes, the induced velocities associated with the vortex sheet as calculated approach infinite magnitudes at the ends of the sheet (at the wall boundary layers), and consequently require some "principal-value" correction. For similar types of non-exact vortex-theory analysis, therefore, it may be desirable to exercise caution in applying the values of induced velocities obtained directly from the theoretical developments in the absence of experimental correlation. The need for empirical correction factors for use with the theoretical induced velocity expressions of the isolated airfoil approach is recognized in reference 22. It is quite probable that the required correlation factor may vary for cascades with widely different geometries (solidity, spacing, and aspect ratio) or for different arrangements of the superimposed vortex system. Further investigation would be necessary to establish the limitations of the method.

CONCLUDING REMARKS

Secondary flows or deviations of the actual flow from distributions determined from considerations of blade-element flow were shown to exist in conventional annular cascades of inlet guide vanes with end-wall boundary layers. In the wall boundary-layer regions, the secondary flows were characterized by a tendency toward underturning near the free-stream side of the boundary layer, toward overturning near the end walls, and by a displacement of the wall boundary layers toward the suction surfaces of the blades. Over the main portion of the flow (potential-flow region), the secondary flows were explained on the basis of the existence of radial variations of the difference

in radial velocity from blade to blade and the requirements of irrotationality. Nonuniform radial velocities were shown to arise from the boundary conditions imposed by the end walls and the thickening of the wall boundary layers over the suction surface.

When large radial gradients of circulation are prescribed, the effects of the secondary flows, exclusive of considerations of the wall boundary layers, are such as to cause a reduction in the magnitude of the gradients near the blade ends; that is, the flow tends to approach the free-vortex condition. The wall boundary layers always tend to reduce the magnitude of the circulation and turning angle as the boundary layers are approached. For vane designs approaching wheel-type outlet rotations, the induced deflections in the tip region of the vanes become especially pronounced. In general, it is unlikely that any arbitrarily specified design variation of turning angle can be obtained along the entire radial height of an annular cascade.

Reductions in the secondary flows in inlet guide vanes are always desirable in compressor and turbine design in order to minimize the induced losses in the vane end regions. Secondary flows can be reduced to a large extent through reductions in the thickness of the annulus-wall boundary layers (fig. 17). Reductions in boundary-layer thickness can be accomplished by careful design of the annulus inlet section and by boundary-layer removal. Methods of boundary-layer removal, however, are costly and rather difficult for inlet guide vanes. For designs with large radial gradients of design circulation, wall boundary-layer removal will not be effective in eliminating the effects of the vorticity in the central region of the vanes. For such cases, information concerning the magnitudes of guide-vane induced losses is necessary in order to evaluate properly the net benefit obtained from the attempted establishment of such design gradients.

It is also probable that the geometry of the cascade configuration selected to produce a given velocity diagram exerts an influence on the magnitude of the secondary losses, for the magnitudes and gradients of the radial velocities will be affected by such factors as chord length, camber, thickness, and spacing. For example, an examination of the terms for spanwise velocity in current boundary-layer secondary flow theory reveals that (within the assumptions of the theory) for fixed flow conditions, the gradient of spanwise velocity across the blade spacing decreases with increasing spacing. It is therefore conceivable that for a given blade height and design velocity diagram, there may exist an optimum combination of blade camber, solidity, and aspect ratio that results in minimum over-all losses.

The existence of trailing vorticity behind the guide-vane row when secondary flows are present means that the flow entering the succeeding rotor row cannot truly be considered irrotational.

However, it is not known to what extent the usual values of guide-vane trailing vorticity will affect the flow and vorticity distributions through the rotor and succeeding stages.

As far as blade-row mismatching due to secondary-flow deflections is concerned, in general, the effects of inlet-guide-vane induced flows on the inlet velocity diagrams relative to a succeeding rotor row, at design conditions do not appear to be as marked as the induced effects on the guide-vane-outlet flow itself. For conventional conservative compressor and turbine designs, the relative induced deflections may not be sufficiently serious to warrant adjustments in the design of the rotor row. For high-performance stages operating at high levels of blade loading and Mach number or for rotors with relatively low stagger angles, however, the secondary flow deflections in the blade end regions may approach significant magnitudes. In such cases, when the inlet-guide-vane design involves either relatively large magnitudes or large radial gradients of turning or both, it may be desirable to affect adjustments in the guide-vane or rotor design in order to account for the velocity diagram distortions.

A relatively simple method of correction, so far as a design procedure is concerned, is to adjust the guide-vane design to compensate for overturning or underturning - as the case may be - in the regions of the vane where such deviations are anticipated. For guide-vane designs similar to those investigated, the calculation method presented can be reliably used to obtain an evaluation of the induced deflections and required adjustments. Adjustments of this nature, however, further increase the magnitudes and gradients of the design circulation, which result in further increases in the secondary flows and losses. The net gain involved in the adjustment is therefore questionable and cannot be evaluated until an indication of the induced losses is obtained. In addition, alteration of the design circulation in one region of a vane will affect the induced velocities in all regions of the vane. The problem therefore is quite complex and would require further investigation before any reliable recommendations could be made.

Lewis Flight Propulsion Laboratory,
National Advisory Committee for Aeronautics,
Cleveland, Ohio.

APPENDIX A

SYMBOLS

The following symbols are used in this report:

| | |
|----------------------------------|--|
| A | annulus area |
| a,b,c | constants |
| C,C ₁ ,C ₂ | correlation or correction factor |
| d | radial distance to axis of boundary-layer vortex core |
| e | distance from annulus wall to axis of boundary-layer vortex core |
| f | $\cos \epsilon = \cos \frac{2\pi j}{N}$ |
| H | total enthalpy |
| h | normal distance between point and vortex axis |
| j,k | integers |
| K | contraction coefficient |
| M | Mach number |
| N | number of vanes in cascade |
| n | polytropic exponent |
| P | point at which induced velocity is calculated |
| p | static pressure |
| q | induced velocity |
| r | radius |
| S | entropy |
| s | direction normal to streamline |
| T | absolute temperature |

| | |
|---------------|--|
| V | velocity |
| x | distance along span |
| z | axial direction |
| β | air exit angle |
| Γ | circulation |
| Δ | change in |
| $\Delta\beta$ | air turning angle |
| δ | boundary-layer thickness |
| ϵ | angle between plane of reference vane and plane of vane containing vortices in question, $j\frac{360}{N}$ |
| θ | circumferential direction |
| ν | angle between line from axis of rectilinear vortex to point in plane of vane and line normal to plane of vane |
| ξ | vorticity parallel to flow |
| ρ | density |
| φ | camber angle for circular-arc camber-line vane |

Subscripts:

| | |
|---|------------------------------------|
| 1 | cascade inlet |
| 2 | cascade outlet (measuring station) |
| b | streamline across vane |
| c | curvature |
| d | design data |
| e | blade element |
| h | hub (inner wall) |
| i | induced |

j,k integers
m mean radius
n normal to plane of trailing vorticity
p point at which induced velocity is calculated
r radial
t tip (outer wall)
w boundary
z axial
 θ tangential

Superscript:

' vortex images or vane trailing edge

APPENDIX B

CALCULATION OF OUTLET VELOCITY AND CIRCULATION

The radial variation of axial and tangential velocity leaving an annular row of blades was obtained from the radial component of the equation of motion given in reference 23 (equation (7d)) for steady axially symmetric flow neglecting terms involving viscosity, or

$$\frac{\partial H}{\partial r} = T \frac{\partial S}{\partial r} + V_{\theta} \frac{\partial V_{\theta}}{\partial r} + V_z \frac{\partial V_z}{\partial r} + \frac{V_{\theta}^2}{r} - V_z \frac{\partial V_r}{\partial z} \quad (B1)$$

For flow across inlet guide vanes, total enthalpy and entropy variations along the radial height can be considered negligible, making $\partial H / \partial r = 0$ and $T \frac{\partial S}{\partial r} = 0$. In addition, the effect of radial accelerations due to variations of the radial velocity component can be neglected with little error (simple radial pressure equilibrium). Equation (B1) then becomes

$$V_z \frac{\partial V_z}{\partial r} = - V_{\theta} \frac{\partial V_{\theta}}{\partial r} - \frac{V_{\theta}^2}{r} \quad (B2)$$

For guide vanes with axial air inlet, the axial and tangential velocities are related through the turning (outlet) angle where

$$V_{\theta} = V_z \tan \beta \quad (B3)$$

Substituting in equation (B2), rearranging, and reducing give

$$\frac{1}{V_z} \frac{\partial V_z}{\partial r} = - \tan \beta \frac{\partial \beta}{\partial r} - \frac{\sin^2 \beta}{r} \quad (B4)$$

Integrating along the radius in terms of the hub reference radial position gives, at fixed axial position,

$$\ln \frac{V_z}{V_{z,h}} = \ln \frac{\cos \beta}{\cos \beta_h} - \int_{r_h}^r \frac{\sin^2 \beta}{r} dr$$

or

$$\frac{V_z}{V_{z,h}} = \frac{\cos \beta}{\cos \beta_h} e^{-\int_{r_h}^r \frac{\sin^2 \beta}{r} dr} \quad (B5)$$

From continuity, across the vane row

$$\int_{r_{1,h}}^{r_{1,t}} V_{z,1} \rho_1 r_1 dr_1 = K \int_{r_h}^{r_t} V_z \rho r dr \quad (B6)$$

where K is a contraction coefficient that accounts for the change in effective flow area from inlet to outlet due to vane wakes and change in wall boundary-layer displacement thickness. For essentially uniform inlet conditions, equation (B6) can be expressed as

$$V_{z,1} \left(\frac{r_{1,t}^2 - r_{1,h}^2}{2} \right) = K V_{z,h} \int_{r_h}^{r_t} \frac{V_z}{V_{z,h}} \frac{\rho}{\rho_1} r dr \quad (B7)$$

The density ratio can be derived from the energy equation and polytropic relation between pressure and density as

$$\frac{\rho}{\rho_1} = \left[1.0 - \frac{\gamma-1}{2} M_1^2 \left(\frac{V^2}{V_1^2} - 1.0 \right) \right]^{\frac{1}{n-1}} \quad (B8)$$

where n is the polytropic exponent for expansion.

Thus, from equations (B5) and (B7), when $V_{z,h}$ is determined, all velocity components can be calculated. The outlet velocity and vane circulation are then obtained from

$$V = \frac{V_{z,h}}{\cos \beta} \left(\frac{V_z}{V_{z,h}} \right) \quad (B9)$$

and

$$\Gamma = \frac{2\pi r}{N} V \sin \beta \quad (B10)$$

For given inlet conditions and radial variation of turning angle, equations (B5) and (B7) were first solved using $K = 0.97$ and $n = 1.39$ (corresponding to a polytropic efficiency of approximately 0.98), and assumed values of ρ/ρ_1 . Values of ρ/ρ_1 were then computed from equation (B8) for the calculated values of velocity obtained from the assumed density ratios in equation (B7). The resulting values of ρ/ρ_1 were then inserted in equation (B7) and new values of velocity were obtained. In all cases, it was unnecessary to compute $V_{z,h}$ more than twice.

APPENDIX C

BLADE-ELEMENT TURNING-ANGLE CORRECTION FOR CIRCULAR-ARC

VANES WITH HUB TAPER

The vanes with circular-arc camber lines used in the investigation had variable chord length and were set in convergent annuli. Blade-element turning angles along the radial height of the vanes were obtained from the straight-line rule of reference 19. The design rule of reference 19 was deduced from experimental data obtained primarily from the central (mean radius) region of vanes set in convergent annuli. As such, the design data represent turning angles for given vane cambers for conditions of radial displacement and the distance to the measuring station characteristic of the mean-radius region of this type of vane. Because of the variation along the vane height of radial deflection of the streamlines and of distance from trailing edge to measuring station (fig. 18), however, the design rule will not be entirely representative of the flow conditions across elements in the hub and tip regions of the vanes investigated.

If the design rule is considered to represent correctly the turning angle at the mean radius of a vane, for an element of given camber at a given radius, the streamline configuration represented by the design-rule data will appear as indicated by the parallel dashed lines in figure 18. For locations other than the mean radius, at the measuring station C-C angle deviations from design-data values will occur because of differences in: (1) the effective camber across the vane, (2) the change in angular momentum from trailing edge to measuring station, and (3) the change in average axial velocity from trailing edge to measuring station. An approximate correction to the design-rule data was therefore made to take these differences into account.

For a given vane section E-E at radius r near the hub (fig. 18), the design rule predicts the value of turning angle at approximately point d for streamline flow corresponding to D-D. In terms of velocity components, this design-data turning angle can be expressed as

$$\tan \Delta\beta_d = \frac{V_{\theta,d}}{V_{z,d}}$$

At point b in the measuring plane at the same radius, however, a somewhat different turning angle will be obtained because of the streamline path B-B of the actual flow, where

$$\tan \Delta\beta_b = \frac{V_{\theta,b}}{V_{z,b}}$$

Thus,

$$\tan \Delta\beta_b = \left(\frac{V_{z,d}}{V_{z,b}} \right) \left(\frac{V_{\theta,b}}{V_{\theta,d}} \right) \tan \Delta\beta_d \quad (C1)$$

From considerations of conservation of angular momentum from the vane trailing edge to the measuring station, along the design-rule streamline D-D,

$$r_{d'} V_{\theta,d'} = r V_{\theta,d}$$

and along the application streamline B-B,

$$r_{b'} V_{\theta,b'} = r V_{\theta,b}$$

Thus

$$\frac{V_{\theta,b}}{V_{\theta,d}} = \left(\frac{r_{b'}}{r} \right) \frac{V_{\theta,b'}}{V_{\theta,d'}} = \left(\frac{r}{r_{d'}} \right) \frac{V_{z,b'}}{V_{z,d'}} \frac{\tan (\Delta\beta')_b}{\tan (\Delta\beta')_d} \quad (C2)$$

Inasmuch as the trailing-edge slant angle and the difference $r_{d'} - r_{b'}$ are small, $V_{z,b'}$ can be assumed equal to $V_{z,d'}$ and by use of the equivalent design-rule streamline at the mean radius, equation (C2) can be expressed as

$$\frac{V_{\theta,b}}{V_{\theta,d}} = \frac{\left(\frac{r}{r'} \right)_m}{\left(\frac{r}{r'} \right)_b} \frac{\tan (\Delta\beta')_b}{\tan (\Delta\beta')_d} = \frac{\left(\frac{r}{r'} \right)_m}{\left(\frac{r}{r'} \right)_b} \frac{\tan (\Delta\beta')_b}{\tan [(\Delta\beta')_b + \Delta(\Delta\beta')]} \quad (C3)$$

where $\Delta(\Delta\beta')$ is the difference in turning angle at d' and b' . A difference in the turning angles at $r_{b'}$ and $r_{d'}$ occurs because of: (1) the difference in the cylindrical-surface camber of the vane corresponding to the two trailing-edge radii and (2) the difference in the effective camber due to the angle of the streamline displacement across the vane. The difference in turning angle due to the difference in cylindrical-surface camber is given by

$$\Delta(\Delta\beta) = \frac{d(\Delta\beta)}{d\phi} \Delta\phi = \frac{d(\Delta\beta)}{d\phi} \frac{d\phi}{dr} \Delta r$$

which, with the turning-angle slope of the straight-line rule (reference 19), becomes

$$\Delta(\Delta\beta') = 0.985 \frac{d\varphi'}{dr} (r_d' - r_b') \quad (C4)$$

The theoretical correction for change in effective camber was negligible for the guide vanes investigated.

Inasmuch as $\Delta(\Delta\beta)$ is generally small compared with $\Delta\beta'$, an equivalent expression for the tangential-velocity ratio can then be obtained, with negligible error as far as the tangent ratio is concerned, as

$$\frac{v_{\theta,b}}{v_{\theta,d}} = \frac{\left(\frac{r}{r'}\right)_m}{\left(\frac{r}{r'}\right)_b} \frac{\tan \Delta\beta_d}{\tan [\Delta\beta_d + \Delta(\Delta\beta)]} \quad (C5)$$

where $\Delta(\Delta\beta)$ is taken as

$$\Delta(\Delta\beta) = 0.985 \frac{d\varphi}{dr} [(r-r')_b - (r-r')_m] \quad (C6)$$

The axial-velocity ratio between points d and b can be represented by the ratio of the average axial velocities at the points; hence, from continuity,

$$\frac{v_{z,d}}{v_{z,b}} = \frac{\rho_b A_b}{\rho_d A_d} \quad (C7)$$

where A_b and A_d are the annulus areas at points b and d, respectively. The annulus-area ratio of equation (C7) can be related to points along the vane trailing edge where, assuming small change in passage taper between measuring station and trailing edge,

$$\frac{\rho_b A_b}{\rho_d A_d} = \frac{\rho_m' A_m'}{\rho_d' A_d'} \quad (C8)$$

For simplicity, the effect of the density ratio can be replaced approximately by considering the right member of equation (C8) to be equivalent to the annulus-area ratio A_m'/A_b' . Thus, equation (C7) becomes

$$\frac{v_{z,d}}{v_{z,b}} = \frac{(r_t^2 - r_h^2)_m'}{(r_t^2 - r_h^2)_b'} \quad (C9)$$

After equations (C5) and (C9) are substituted into equation (C1), the corrected blade-element turning-angle relation is obtained as

$$\tan \Delta\beta_b = \frac{(r_t^2 - r_h^2)_m \left(\frac{r}{r'}\right)_m}{(r_t^2 - r_h^2)_b \left(\frac{r}{r'}\right)_b} \left\{ \frac{\tan \Delta\beta_d}{\tan [\Delta\beta_d + \Delta(\Delta\beta)]} \right\} \tan \Delta\beta_d \quad (C10)$$

where $\Delta(\Delta\beta)$ is given by equation (C6).

REFERENCES

1. Carter, A. D. S.: Three-dimensional-flow Theories for Axial Compressors and Turbines. War Emergency Issue No. 41 pub. by Inst. Mech. Eng. (London). (Reprinted in U. S. by ASME, April 1949, pp. 255-268.)
2. Wu, Chung-Hua: Survey of Available Information on Internal Flow Losses through Axial Turbomachines. NACA RM E50J13, 1951.
3. Carter, A. D. S., and Cohen, Elizabeth M.: Preliminary Investigation into the Three-dimensional Flow through a Cascade of Aerofoils. R. & M. No. 2339, British A.R.C., Feb. 1946.
4. Howell, A. R.: Fluid Dynamics of Axial-Flow Compressor. War Emergency Issue No. 12 pub. by Inst. Mech. Eng. (London), 1945. (Reprinted in U. S. by ASME, Jan. 1947, pp. 441-452.)
5. Bowen, J. T., Sabersky, R. H., and Rannie, W. D.: Investigations of Axial Flow Compressors. ASME Paper No. 49-A-102, presented before 1949 ASME Annual Meeting, (New York), Dec. 2, 1949.
6. Hausmann, George F.: The Theoretical Induced Deflection Angle in Cascades Having Wall Boundary Layers. Jour. Aero. Sci., vol. 15, no. 11, Nov. 1948, pp. 686-690.
7. Tsien, Hsue-Shen: Loss in Compressor or Turbine Due to Twisted Blades. C.I.E. Jour., 1947, pp. 40-53.
8. Squire, H. B., and Winter, K. G.: The Secondary Flow in Cascade of Aerofoils in Non-Uniform Stream. Rep. No. Aero. 2317, British R.A.E., March 1949.
9. Hawthorne, William R.: Secondary Circulation in Fluid Flow. Gas Turbine Lab. M.I.T., May 1950.
10. Weske, John R.: Fluid Dynamic Aspects of Axial Flow Compressors and Turbines. Jour. Aero. Sci., vol. 14, no. 11, Nov. 1947, pp. 651-656.
11. Emmons, Howard W., and Ball, George A.: The Present Status of Axial Flow Compressor Design. Harvard Univ., NAW-3662, 1947.
12. Mager, Artur: Generalization of Boundary-Layer Momentum-Integral Equations to Three-Dimensional Flows Including Those of Rotating System. NACA TN 2310, 1951.
13. Kantrowitz, Arthur, and Daum, Fred L.: Preliminary Experimental Investigation of Airfoils in Cascade. NACA CB, July 1942.

14. Toussaint, A.: Experimental Methods - Wind Tunnels. Part I. Vol. III of Aerodynamic Theory, div. I, ch. 1, sec. 2, W. F. Durand, ed., Julius Springer (Berlin), 1935, p. 283. (Reprinted, C.I.T., Jan. 1943.)
15. Smith, C. B.: Wind-Tunnel Wall Corrections for Wing-Body Combinations. Jour. Aero. Sci., vol. 16, no. 4, April 1949, pp. 237-242.
16. Glauert, H.: The Elements of Aerofoil and Airscrew Theory. Cambridge Univ. Press (London), 1947, p. 127.
17. Tsien, Hsue-Shen, and Lees, Lester: The Glauert-Prandtl Approximation for Subsonic Flows of a Compressible Fluid. Jour. Aero. Sci., vol. 12, no. 2, April 1945, pp. 173-187, 202.
18. Zimney, Charles M., and Lappi, Viola M.: Data for Design of Entrance Vanes from Two-Dimensional Tests of Airfoils in Cascade. NACA ACR No. L5G18, 1945.
19. Lieblein, Seymour: Turning-Angle Design Rules for Constant-Thickness Circular-Arc Inlet Guide Vanes in Axial Annular Flow. NACA TN 2179, 1950.
20. Huppert, M. C., and MacGregor, Charles: Comparison between Predicted and Observed Performance of Gas-Turbine Stator Blade Designed for Free-Vortex Flow. NACA TN 1810, 1949.
21. Lieblein, Seymour, and Sandercock, Donald M.: Compressibility Correction for Turning Angles of Axial-Flow Inlet Guide Vanes. NACA TN 2215, 1950.
22. Carter, A. D. S.: A Note on the Use of Porous Walls for Cascade Tunnels. Memo No. M. 79, British N.G.T.E., March 1950.
23. Wu, Chung-Hua, and Wolfenstein, Lincoln: Application of Radial-Equilibrium Condition to Axial-Flow Compressor and Turbine Design. NACA Rep. 995, 1950. (Formerly NACA TN 1795.)
24. Mahoney, John J., Dugan, Paul D., Budinger, Raymond E., and Goelzer, H. Fred: Investigation of Blade-Row Flow Distributions in Axial-Flow-Compressor Stage Consisting of Guide Vanes and Rotor-Blade Row. NACA RM E50G12, 1950.

TABLE I - BLADE DESIGN AND ANNULUS DATA

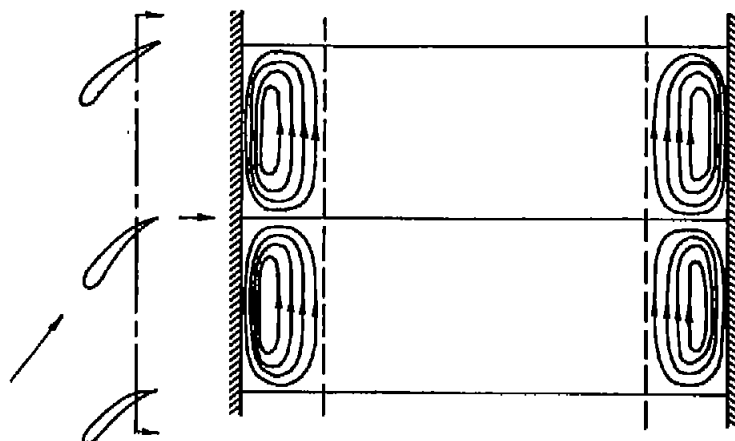


| Guide vane design | Type | Mean line | Thick-ness distri-bution | Average maximum thickness ratio (percent chord) | Chord (in.) | | Average solidity | Radius at tip (in.) | Radius at hub inlet (in.) | Radius at hub outlet (in.) | Aspect ratio | Location of meas-uring station (in.) | Inlet Mach number |
|-------------------|------------|--------------|--------------------------|---|-------------|------|------------------|---------------------|---------------------------|----------------------------|--------------|--------------------------------------|-------------------|
| | | | | | Hub | Tip | | | | | | | |
| A | Compressor | Circular arc | Constant | 3.7 | 1.23 | 2.00 | 1.65 | 7.00 | 3.64 | 4.07 | 2.09 | 0.25 | 0.28 |
| B | Compressor | Circular arc | Constant | 3.7 | 1.23 | 2.00 | 1.65 | 7.00 | 3.64 | 4.07 | 2.09 | .25 | .28 |
| C ¹ | Compressor | Circular arc | Constant | 3.7 | 2.79 | 3.76 | 1.55 | 15.00 | 11.48 | 11.98 | .94 | .25 | .29 |
| D ² | Compressor | 65-series | Variable | 10.0 | 1.75 | 1.75 | 1.3 | 6.59 | 5.10 | 5.10 | .85 | .92 | .60 |
| E | Compressor | 65-series | Constant | 3.1 | 1.65 | 2.18 | 1.0 | 8.00 | 6.00 | 6.00 | 1.04 | .30 | .60 |
| F ³ | Turbine | - - - | Variable | 13.8 | 2.05 | 2.10 | 1.56 | 11.70 | 9.00 | 9.00 | 1.30 | .20 | .20 |

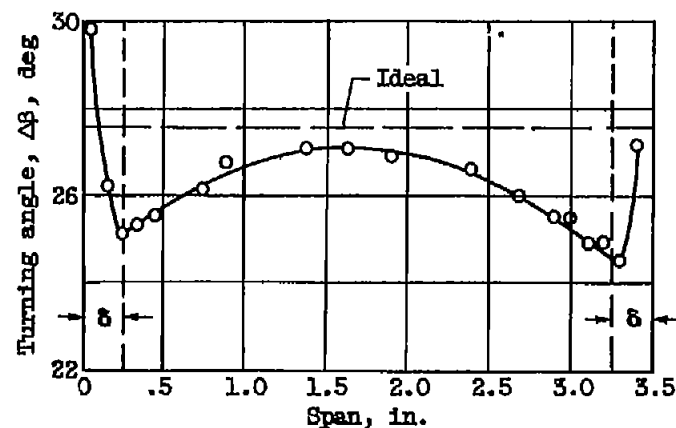
¹Design data obtained from Fredric Fladar, Inc.

²Design data obtained from reference 20.

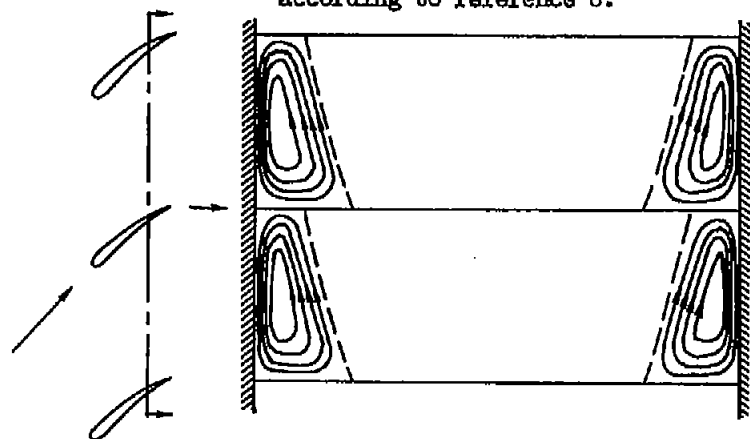
³Design data obtained from reference 24.



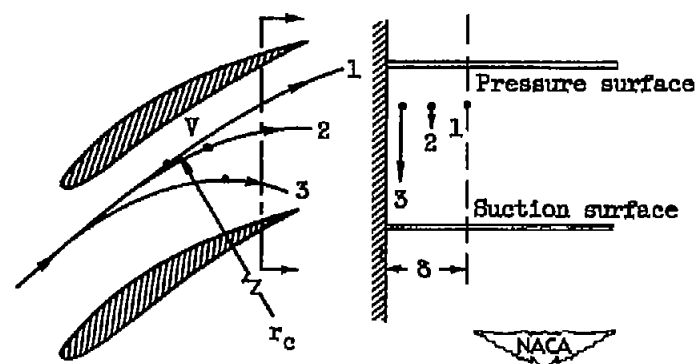
(a) Streamlines of secondary circulation according to reference 8.



(b) Experimental variation of turning angle along span in two-dimensional cascade.

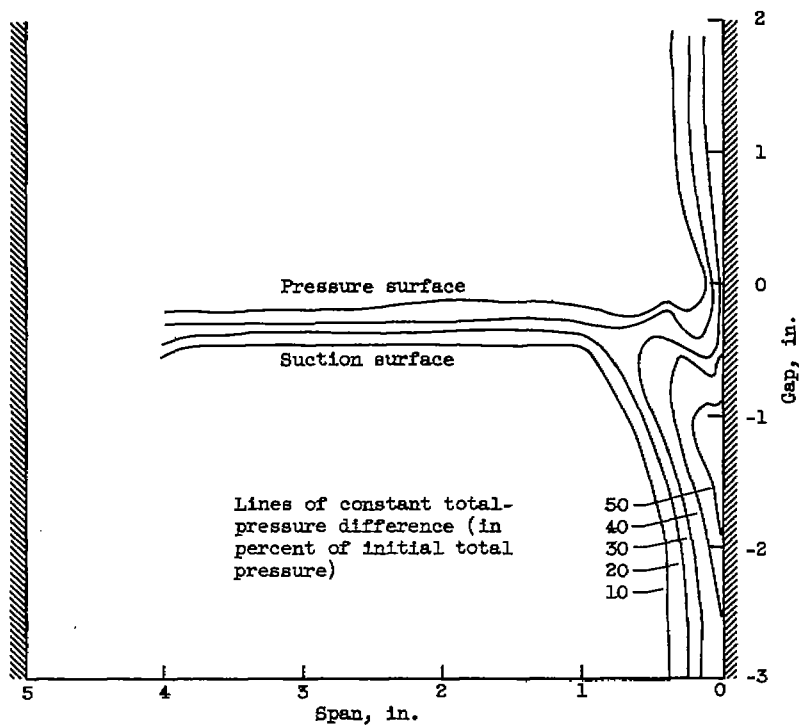


(c) Displacement of boundary layers toward suction surface.

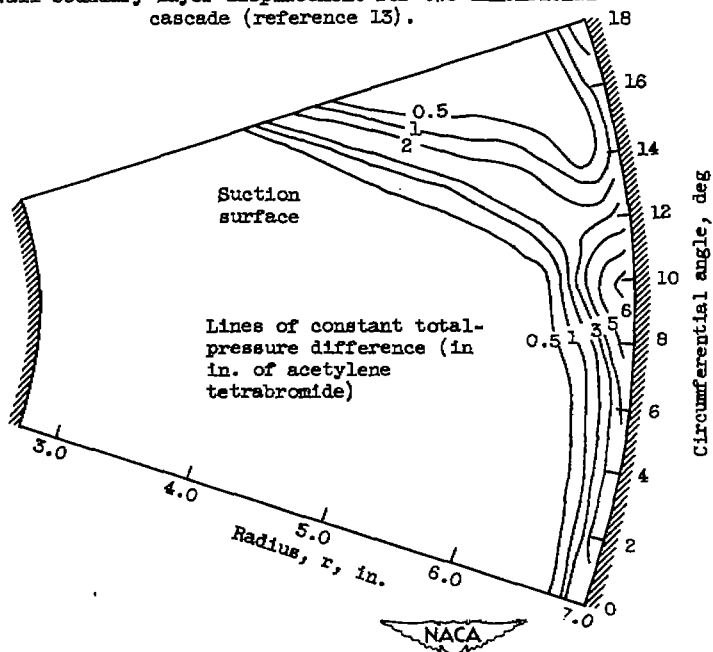


(d) Effect of spacing pressure gradient.

Figure 1. - Secondary flows in wall boundary-layer regions of cascades.



(e) Wall boundary-layer displacement for two-dimensional cascade (reference 13).



(f) Wall boundary-layer displacement for inlet guide vanes.

Figure 1. - Concluded. Secondary flows in wall boundary-layer regions of cascades.

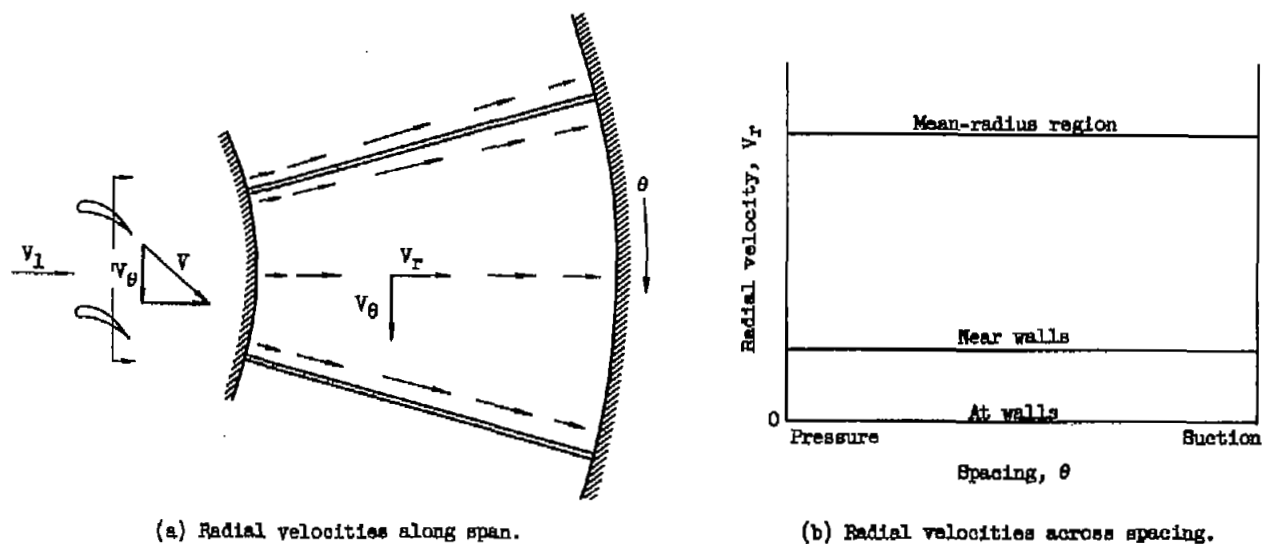


Figure 2. - Radial flows in annular cascades with free-vortex blading and without wall boundary layers.

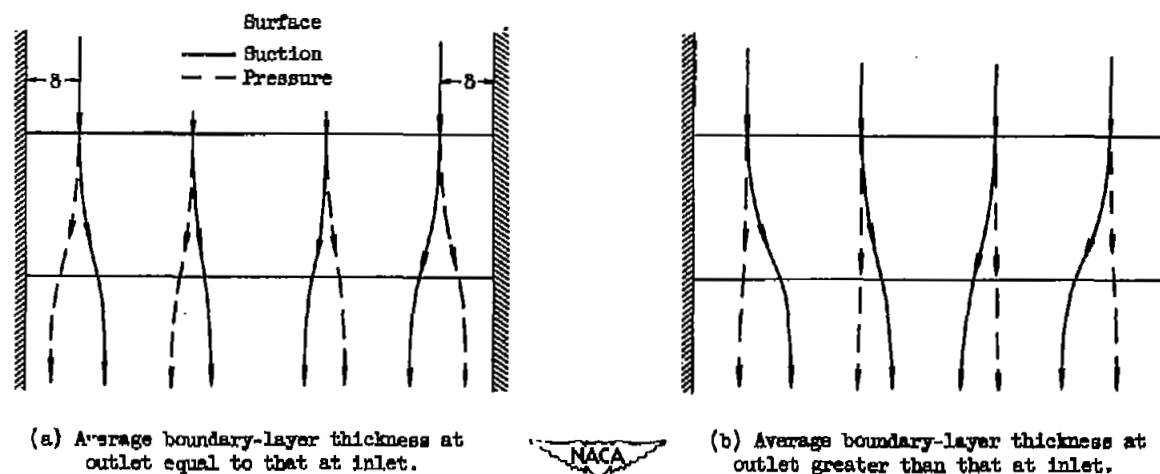
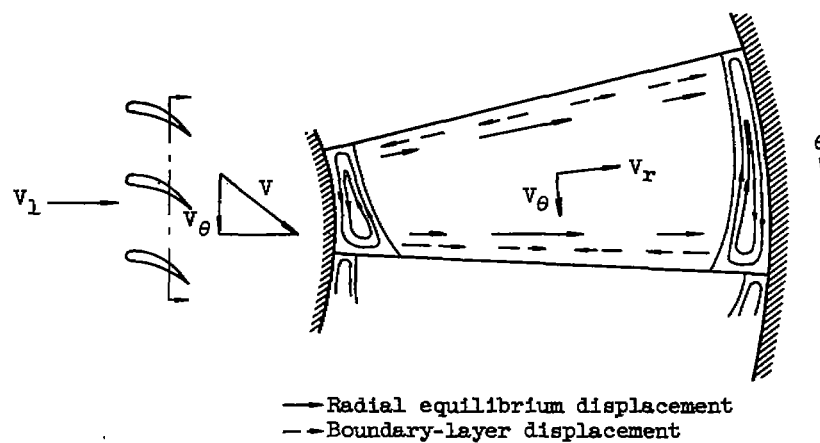
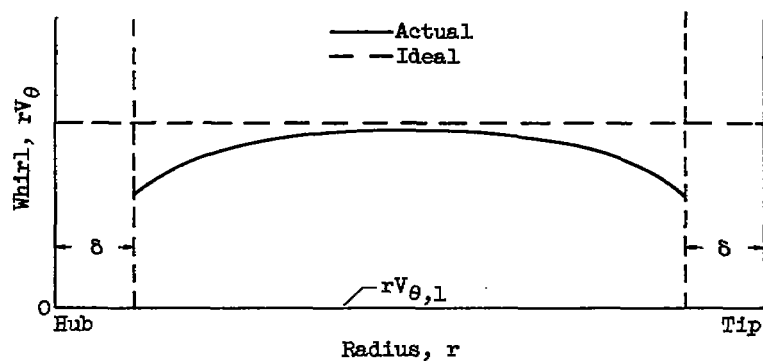


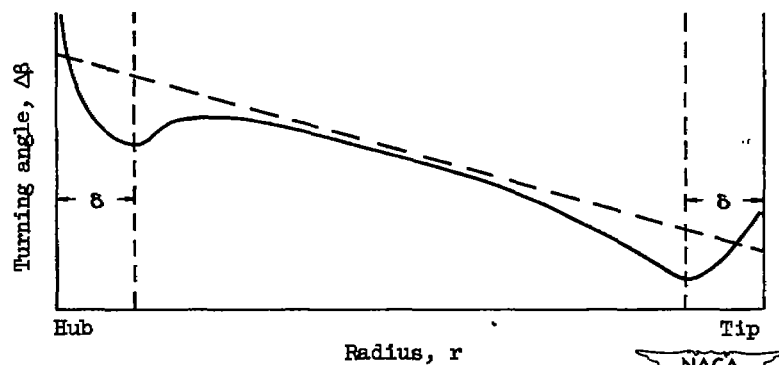
Figure 3. - Displacement of streamlines over blade surfaces due to secondary flow in wall boundary layer.



(a) Radial velocities for accelerating flow.

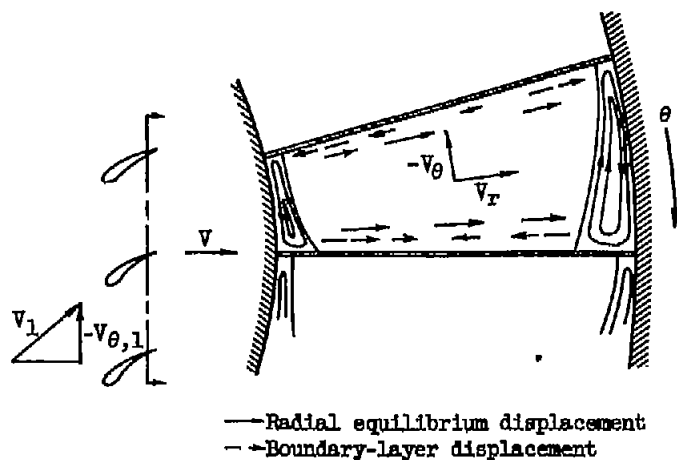


(b) Radial variation of whirl for accelerating flow.

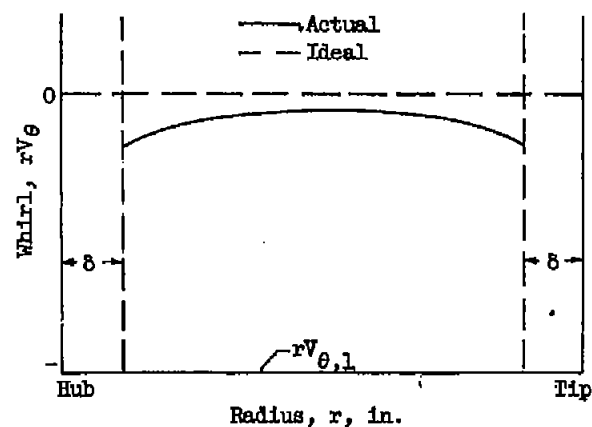


(c) Radial variation of turning angle for accelerating flow.

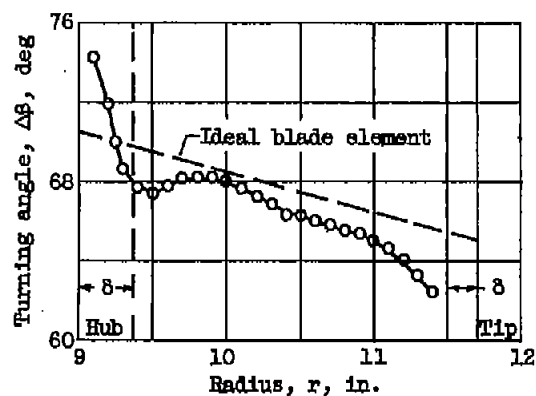
Figure 4. - Secondary flows in annular cascades with free-vortex blading.



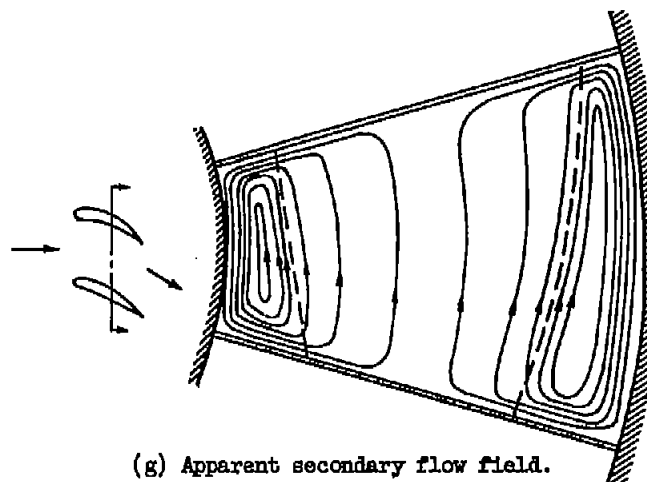
(d) Radial velocities for decelerating flow.



(e) Radial variation of whirl for decelerating flow.

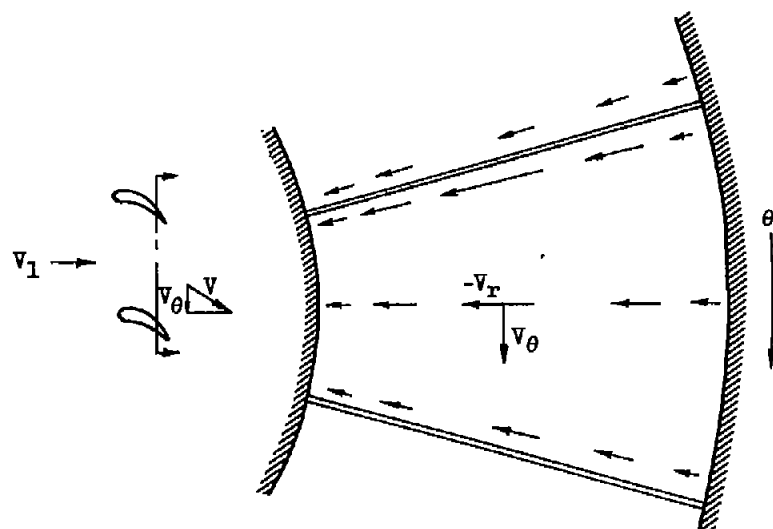


(f) Experimental variation of turning angle across free-vortex turbine-inlet nozzle (reference 20).

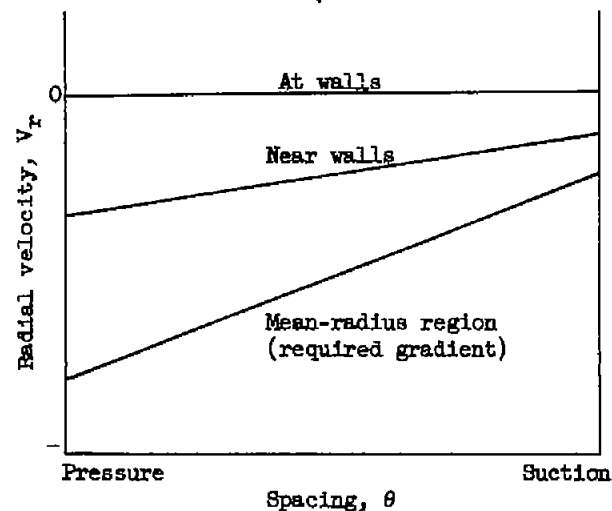


(g) Apparent secondary flow field.

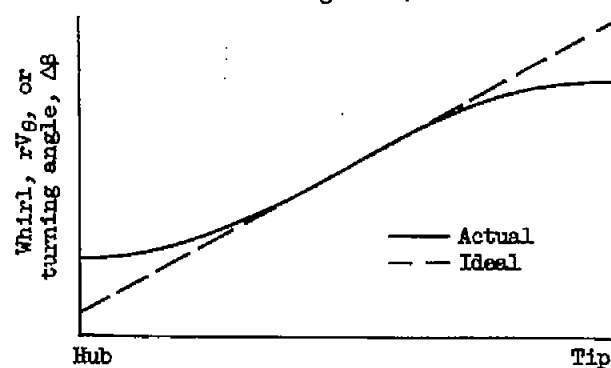
Figure 4. - Concluded. Secondary flows in annular cascades with free-vortex blading.



(a) Radial velocities along span for radially increasing circulation.

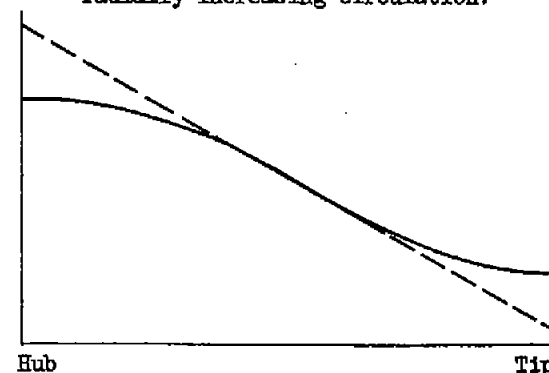


(b) Radial velocities across spacing for radially increasing circulation.



(c) Turning angle and whirl for radially increasing circulation.

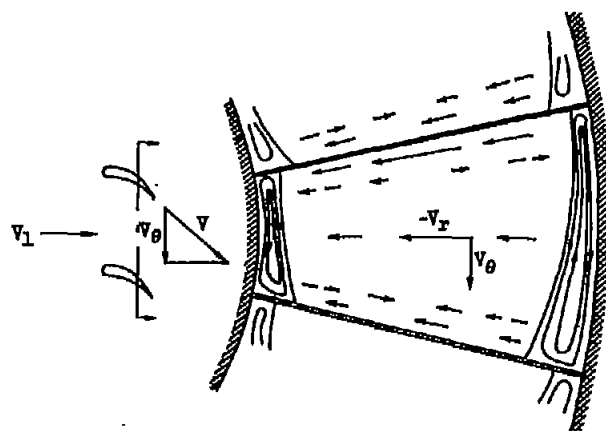
Radius, r



(d) Turning angle and whirl for radially decreasing circulation.

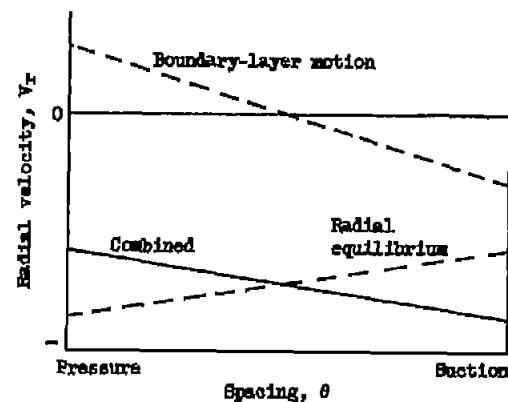


Figure 5. - Secondary flows in annular cascades with radial circulation gradients and without wall boundary layers.

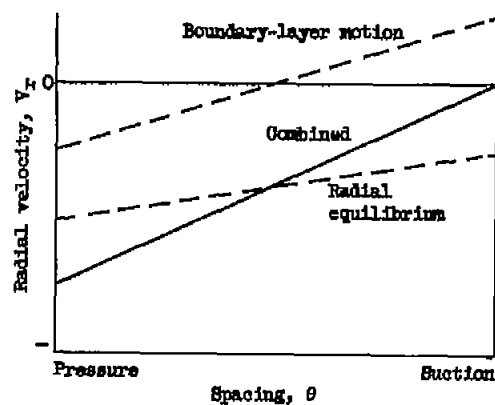


— Radial equilibrium displacement
 - - Boundary-layer displacement

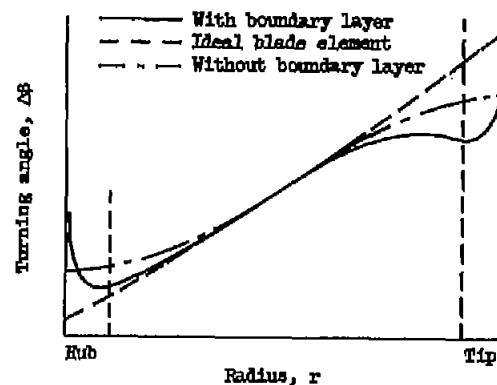
(a) Radial velocities along span.



(b) Radial velocities across spacing in tip region.



(c) Radial velocities across spacing in hub region.



(d) Radial variation of turning angle.



Figure 6. - Secondary flows in annular cascades with radial circulation gradients and with wall boundary layers. Radially increasing circulation (constant tangential velocity).

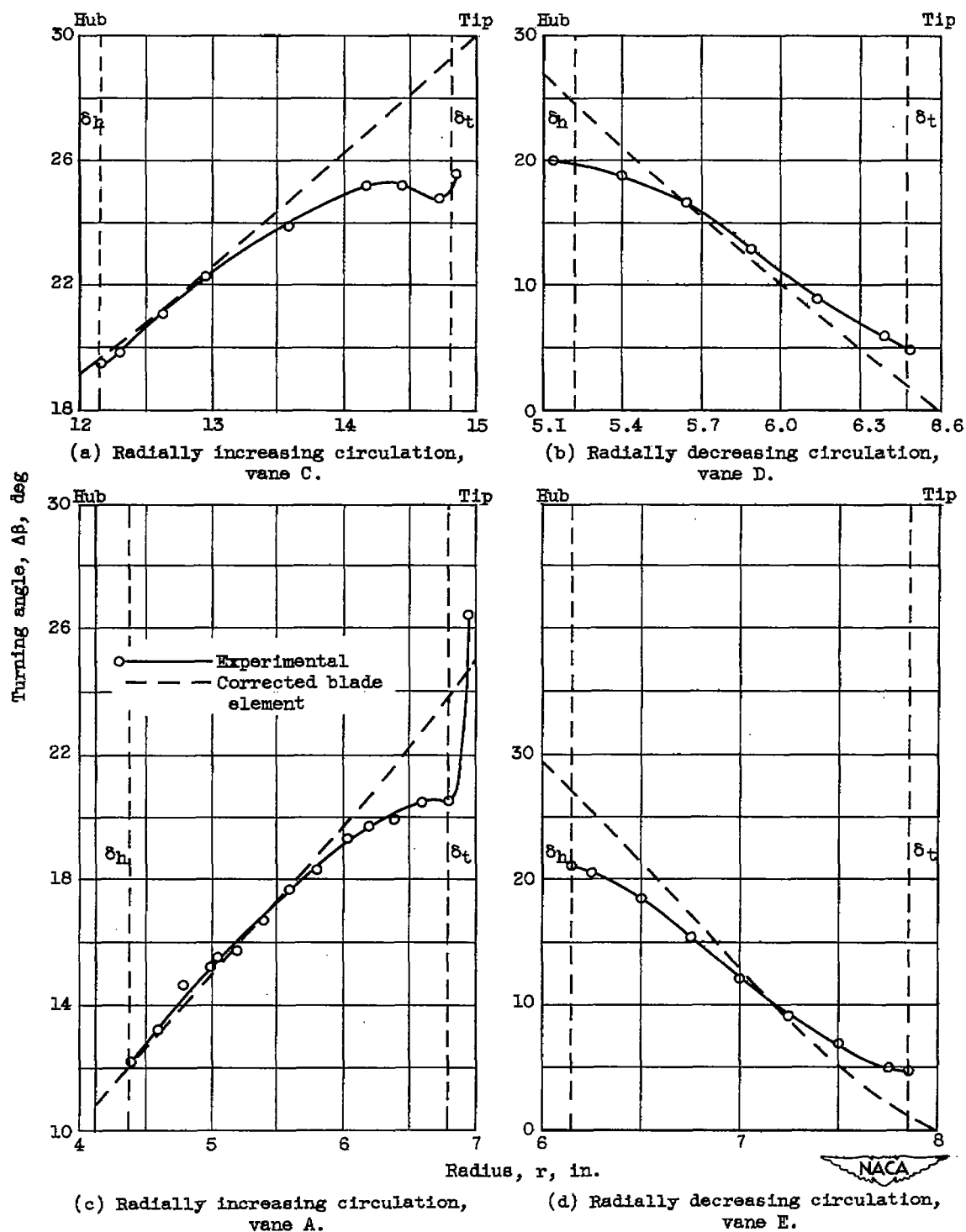


Figure 7. - Experimental variation of air turning angle for inlet guide vanes.

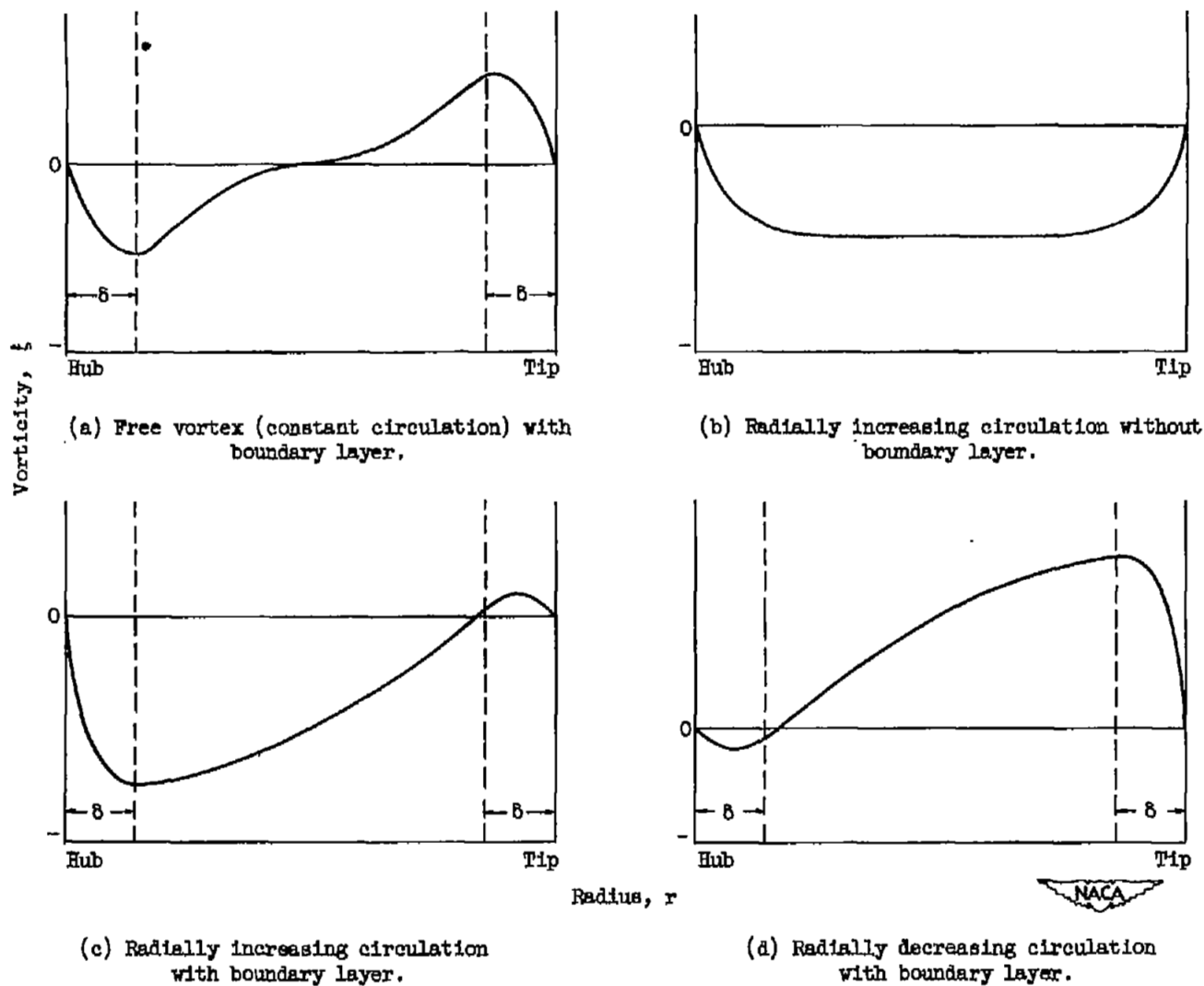
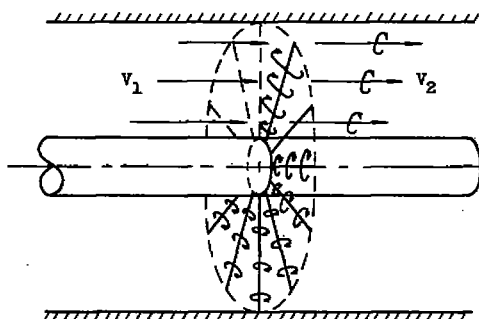
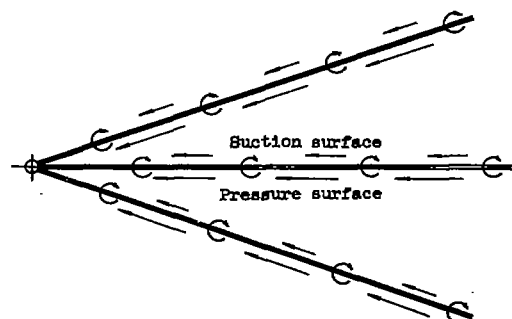


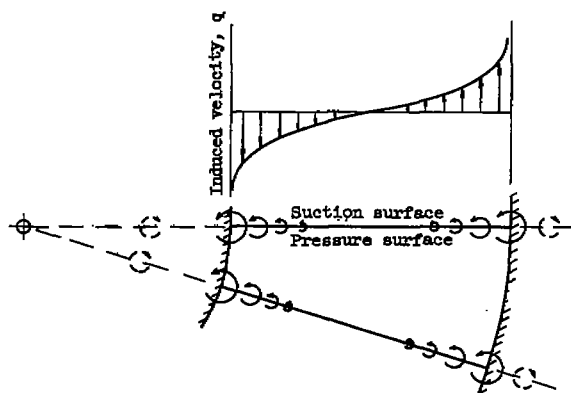
Figure 8. - Qualitative variation of trailing vorticity along span of blades in annular cascade.



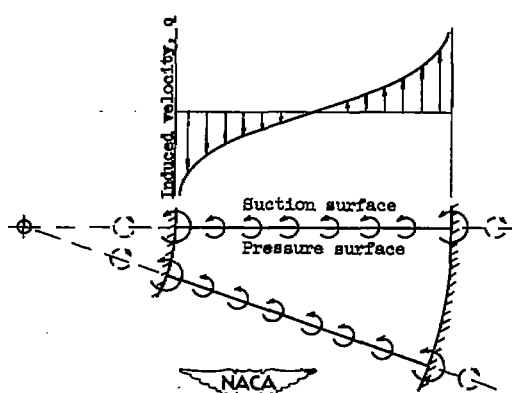
(a) Assumed cascade and flow configuration.



(b) Radial flows in ideal infinite annular flow and corresponding trailing vorticity. Linearly increasing circulation.

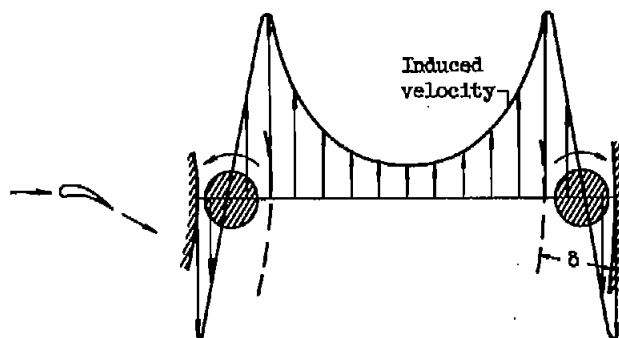


(c) Superimposed vortex system between finite annulus boundaries to approximate true trailing vortex system and true turning angle deflections. Linearly increasing circulation without wall boundary layer.

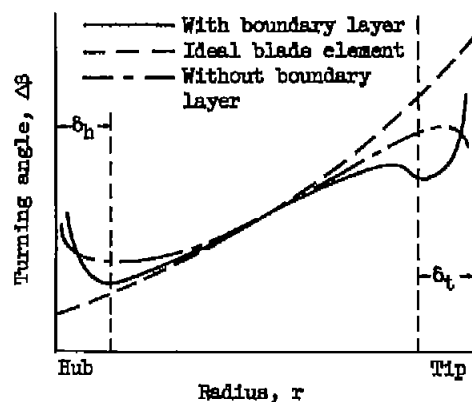


(d) Superimposed vortex system directly proportional to ideal vorticity to approximate true turning-angle deflections with zero net vorticity at boundaries. Linearly increasing circulation without wall boundary layers.

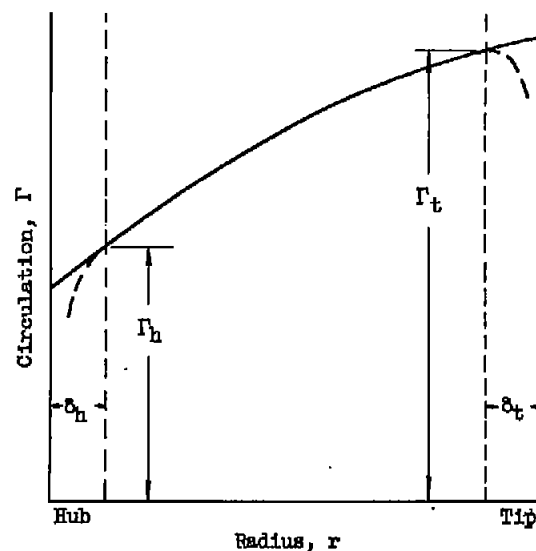
Figure 9. - Development of superimposed vortex system for induced turning-angle correction.



(e) Superimposed circular vortices in wall boundary-layer regions and corresponding induced velocities to approximate secondary-flow effect of wall boundary layers.



(g) Variation of turning angle obtained from induced velocities of superimposed vortex system. Radially increasing circulation.



Circular vortex Vortex sheet Circular vortex

$$\Gamma_h \approx \Gamma_h \quad \Gamma \approx \frac{d\Gamma}{dr} dr \quad \Gamma_t \approx -\Gamma_t$$

(f) Determination of strength of superimposed vorticity from blade-element (design) variation of circulation.



Figure 9. - Concluded. Development of superimposed vortex system for induced turning-angle correction.

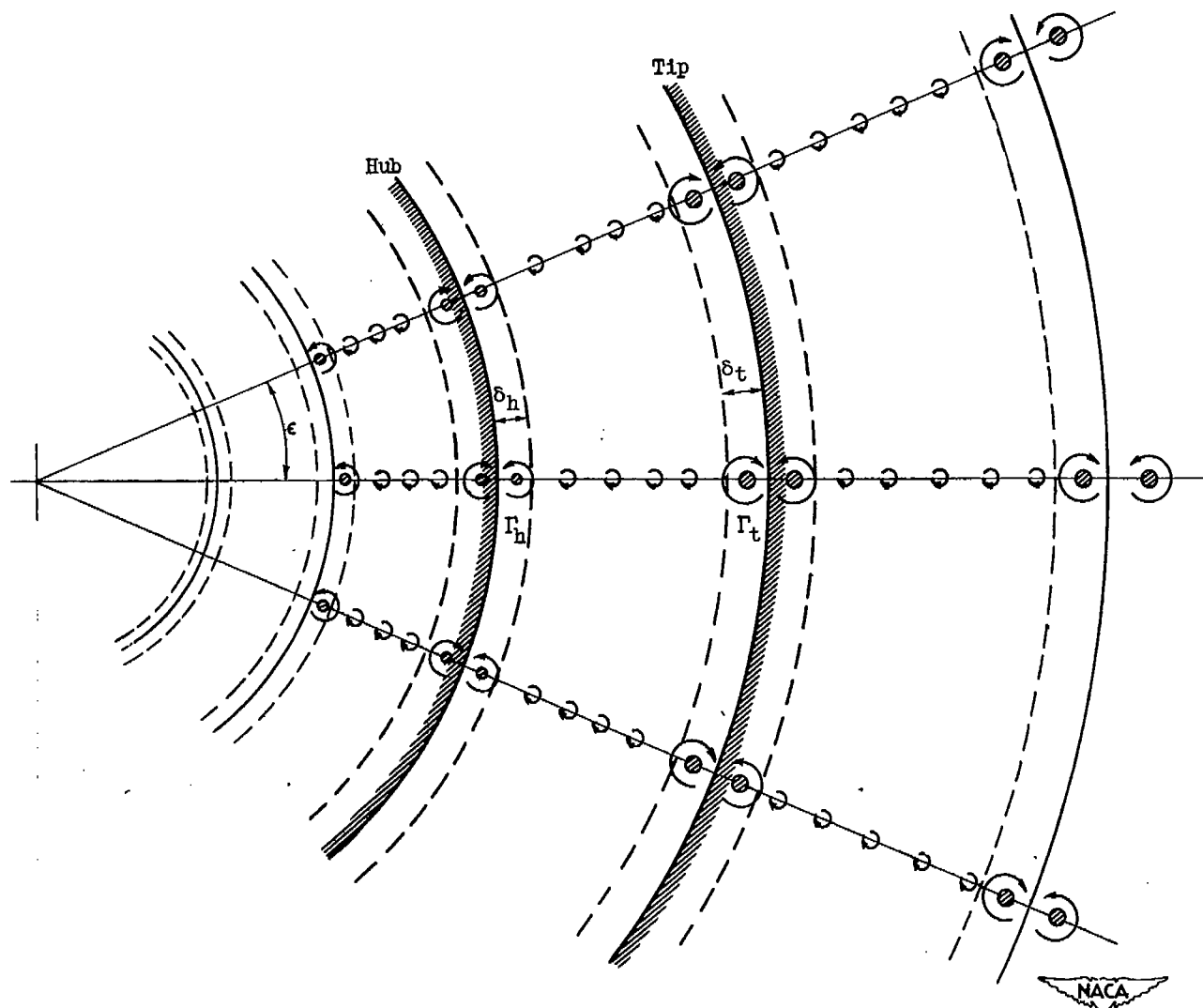


Figure 10. - Partial view of complete superimposed vortex system for induced turning-angle correction.
Radially increasing circulation.

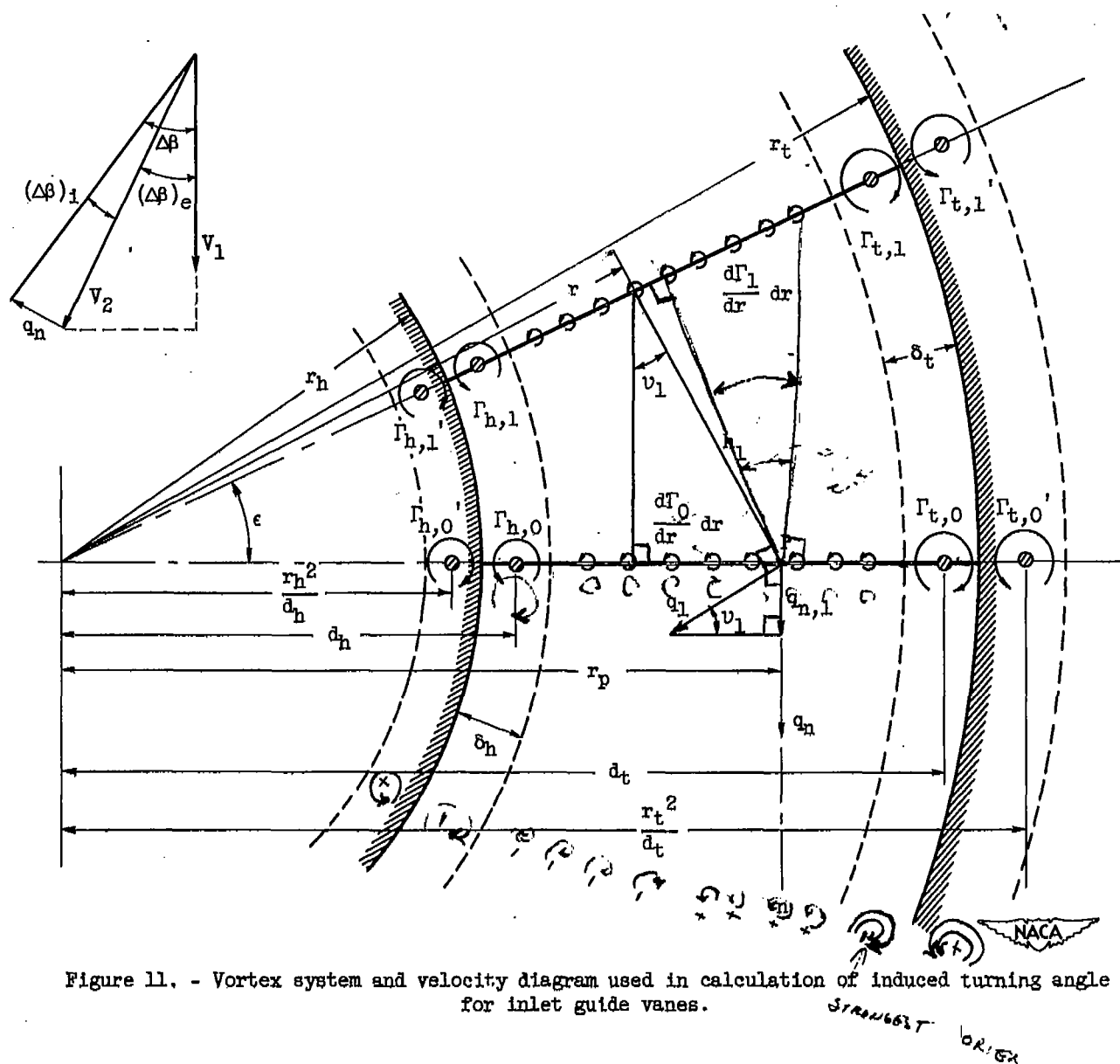


Figure 11. - Vortex system and velocity diagram used in calculation of induced turning angle for inlet guide vanes.

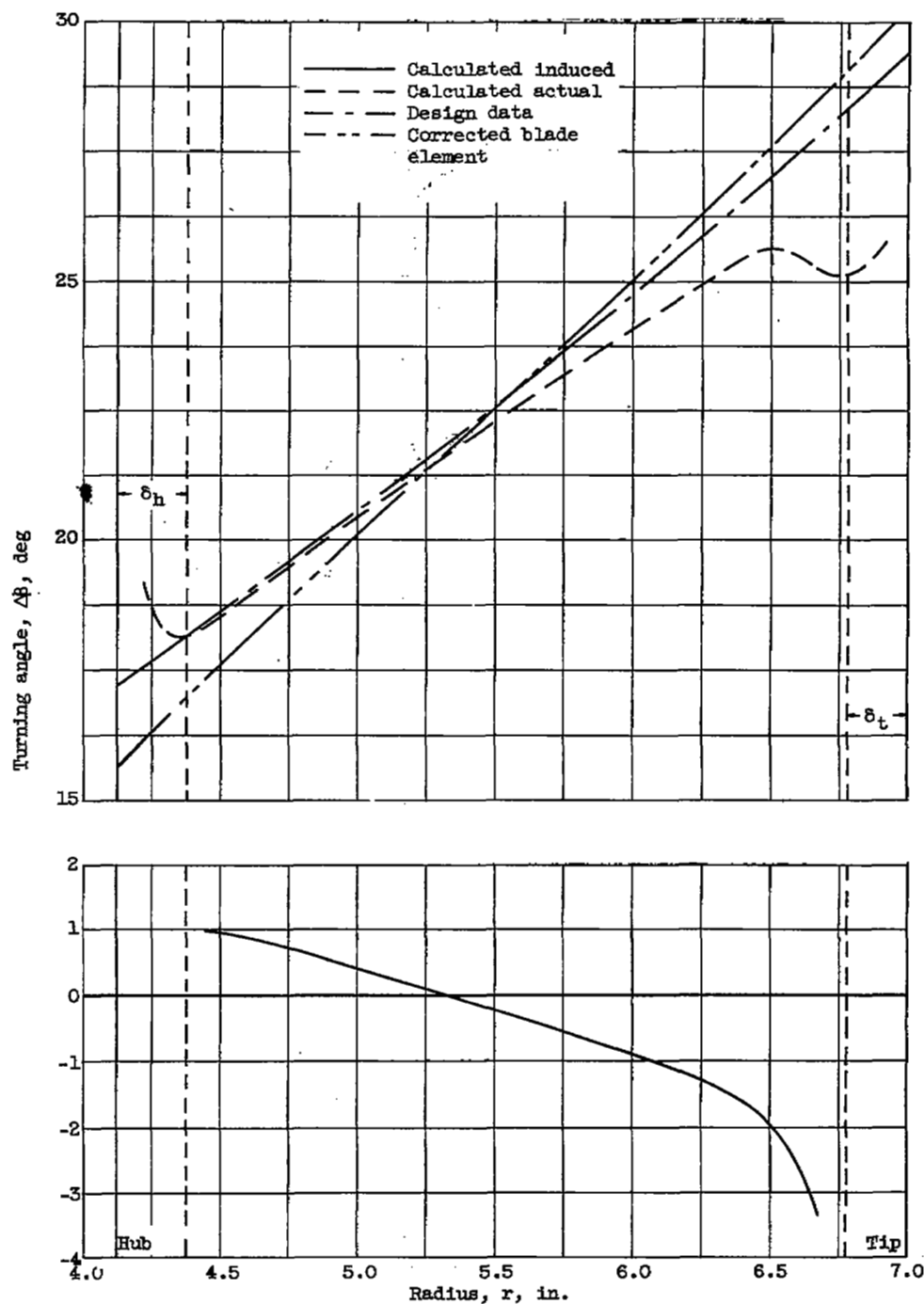


Figure 12. - Illustration of calculated actual turning angle.

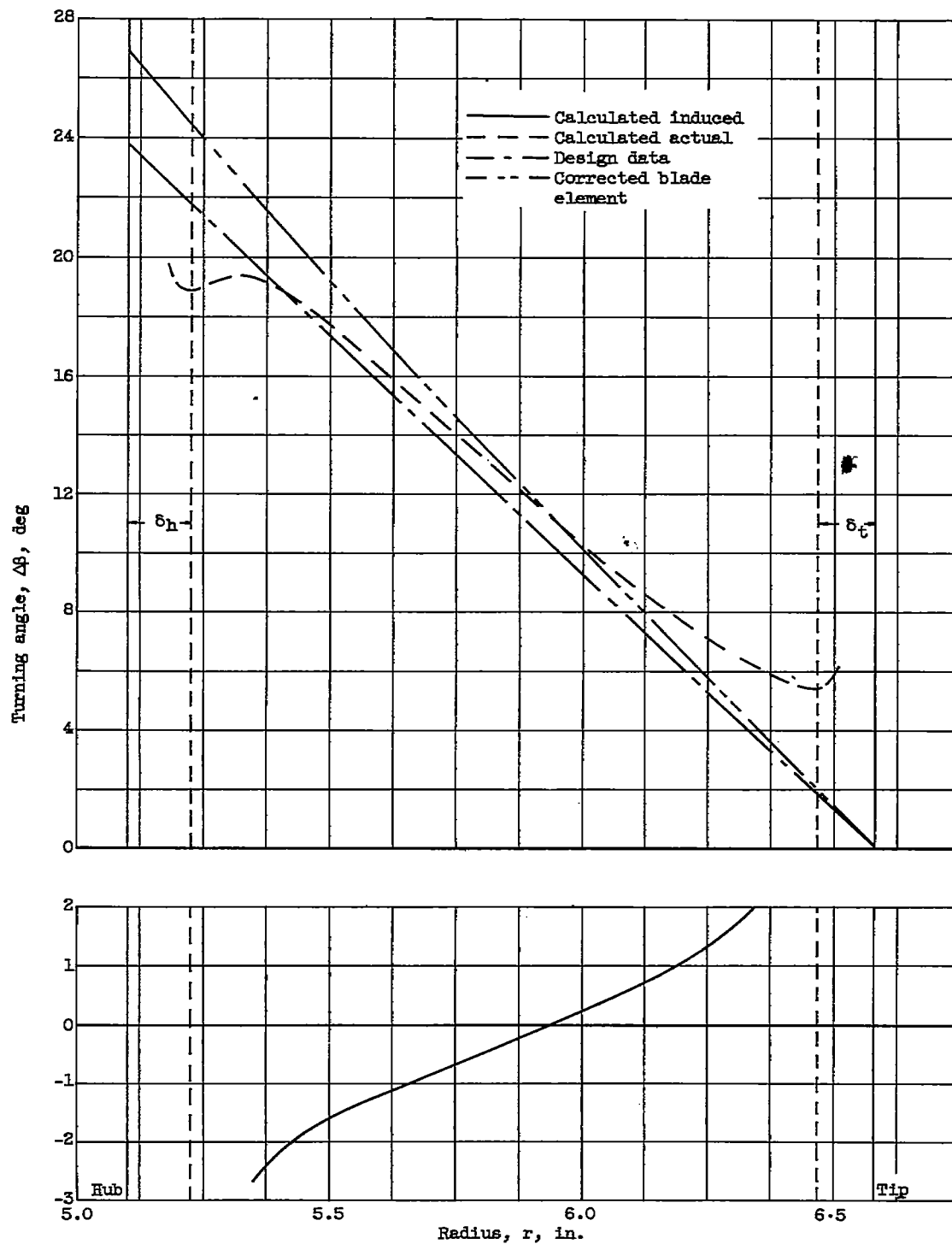


Figure 12. - Concluded. Illustration of calculated actual turning angle.

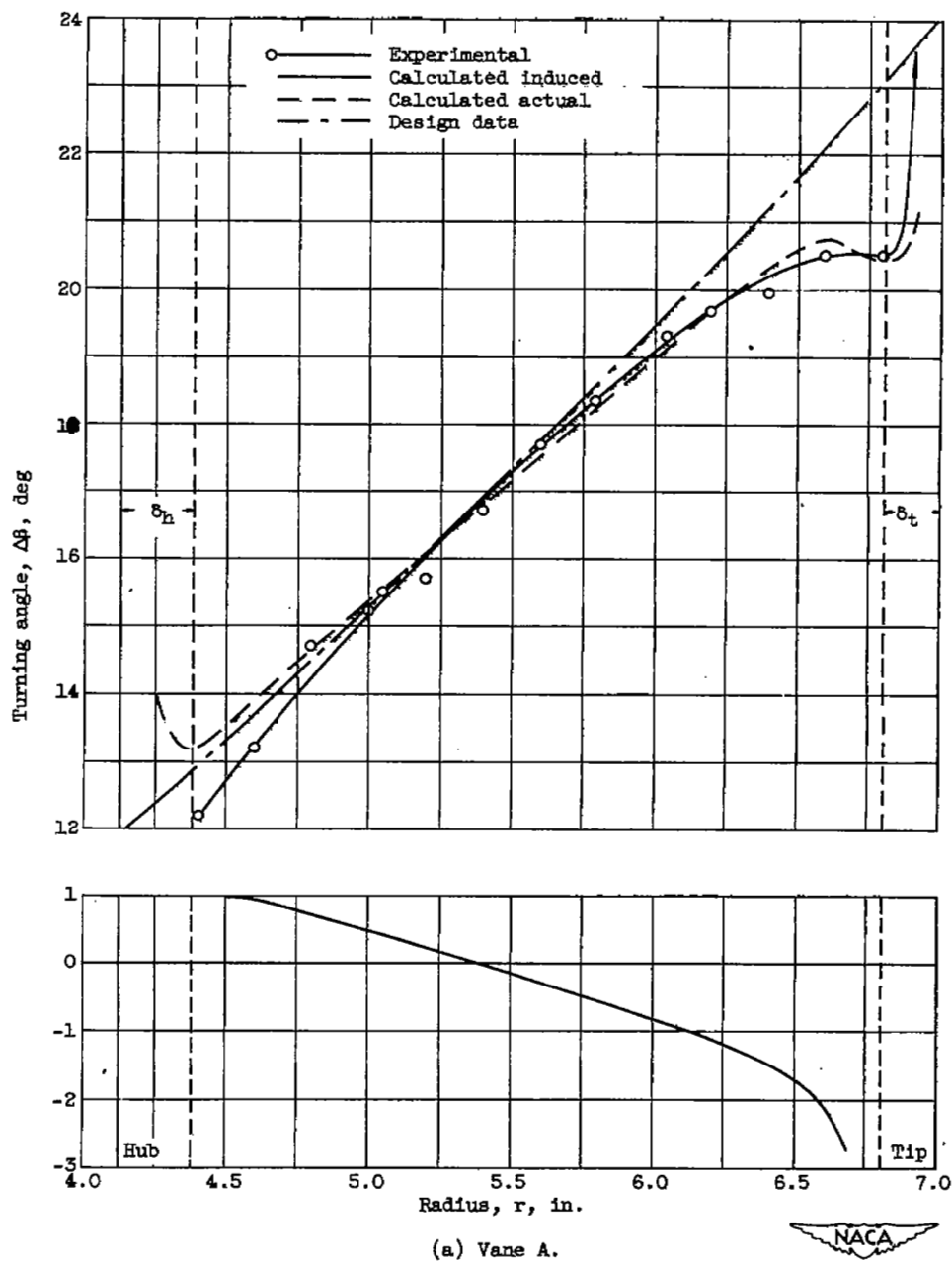
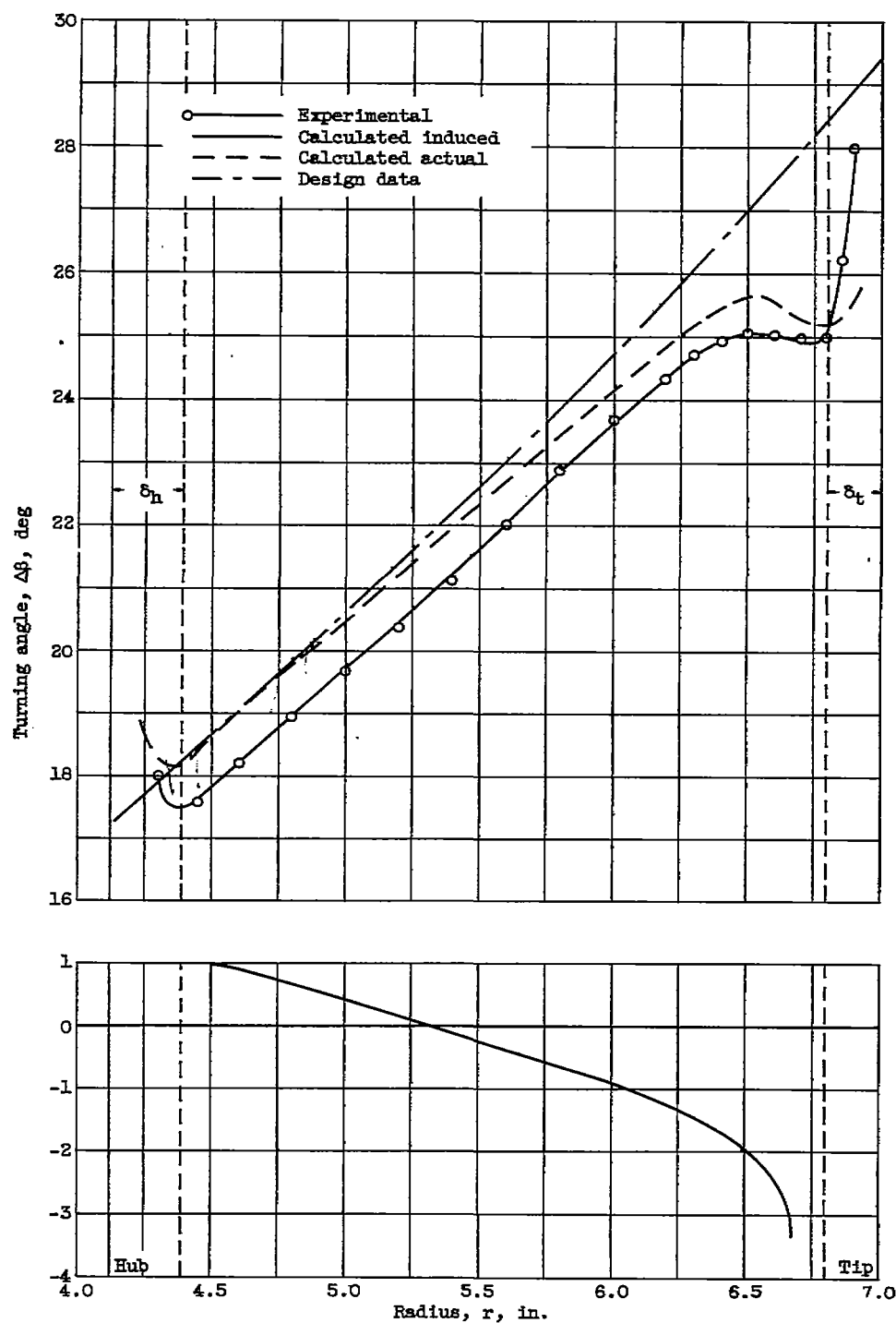


Figure 13. - Comparison of calculated and experimental turning angles of inlet guide vanes.



(b) Vane B.



Figure 13. - Continued. Comparison of calculated and experimental turning angles of inlet guide vanes.

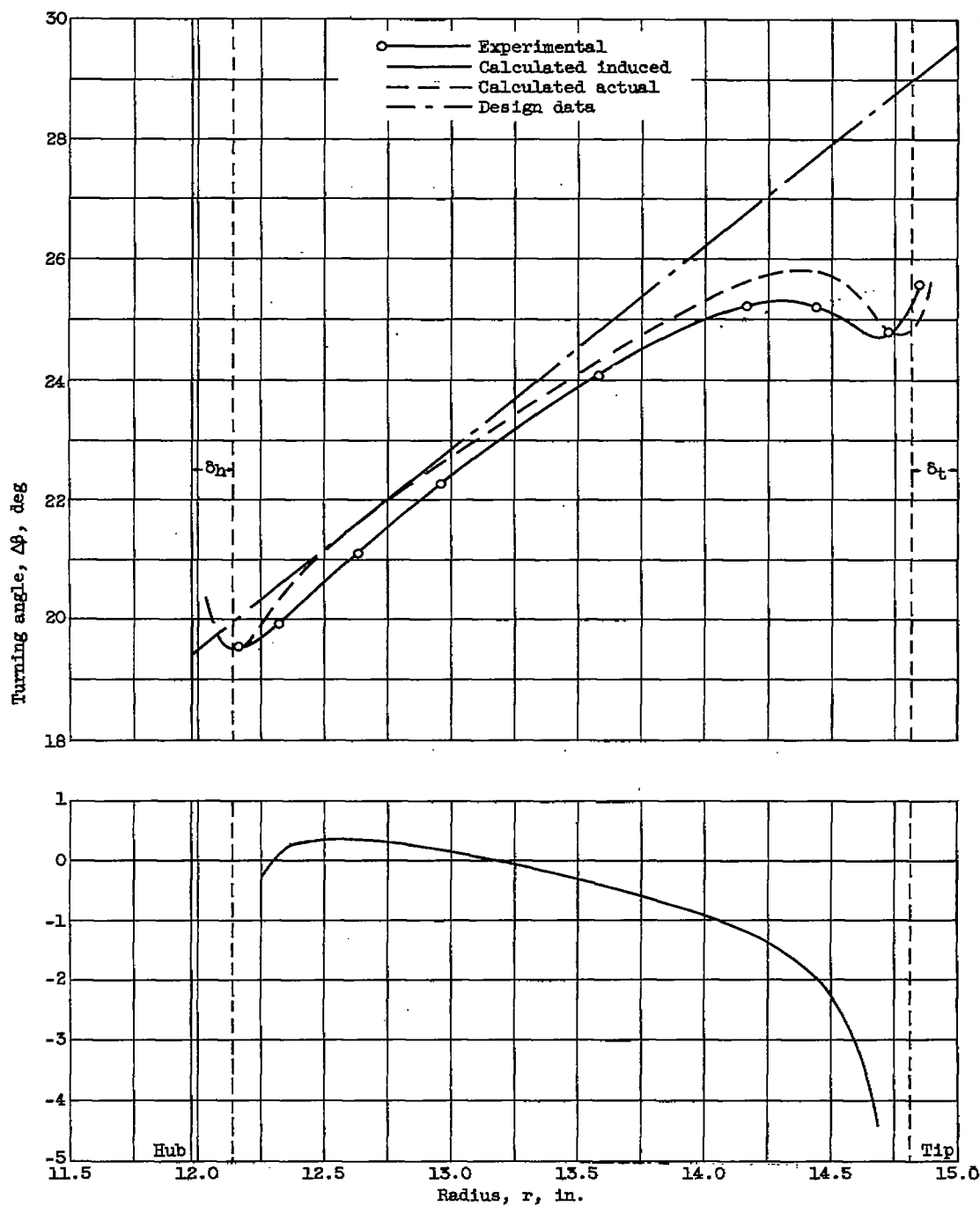


Figure 13. - Continued. Comparison of calculated and experimental turning angles of inlet guide vanes.

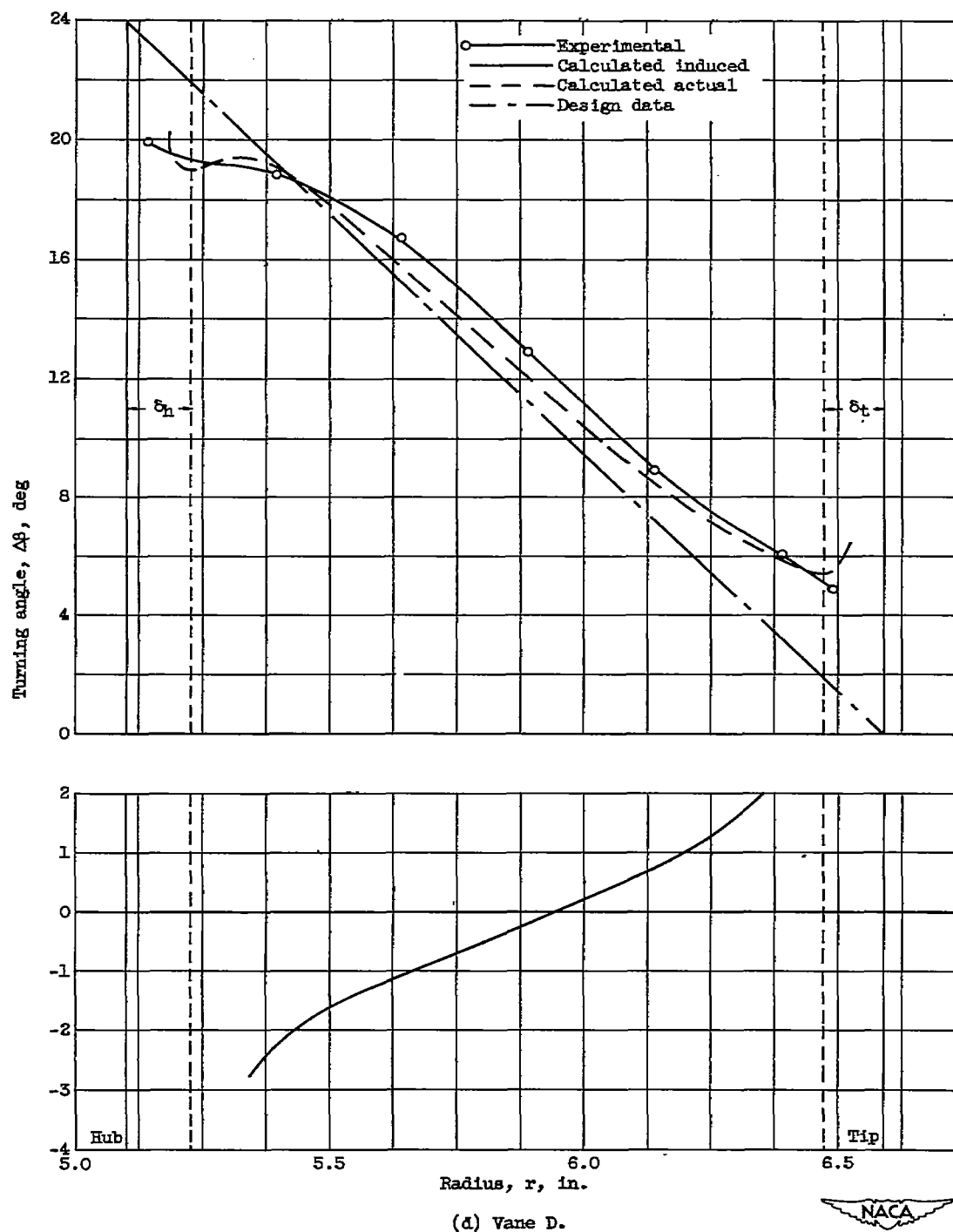


Figure 13. - Continued. Comparison of calculated and experimental turning angles of inlet guide vanes.

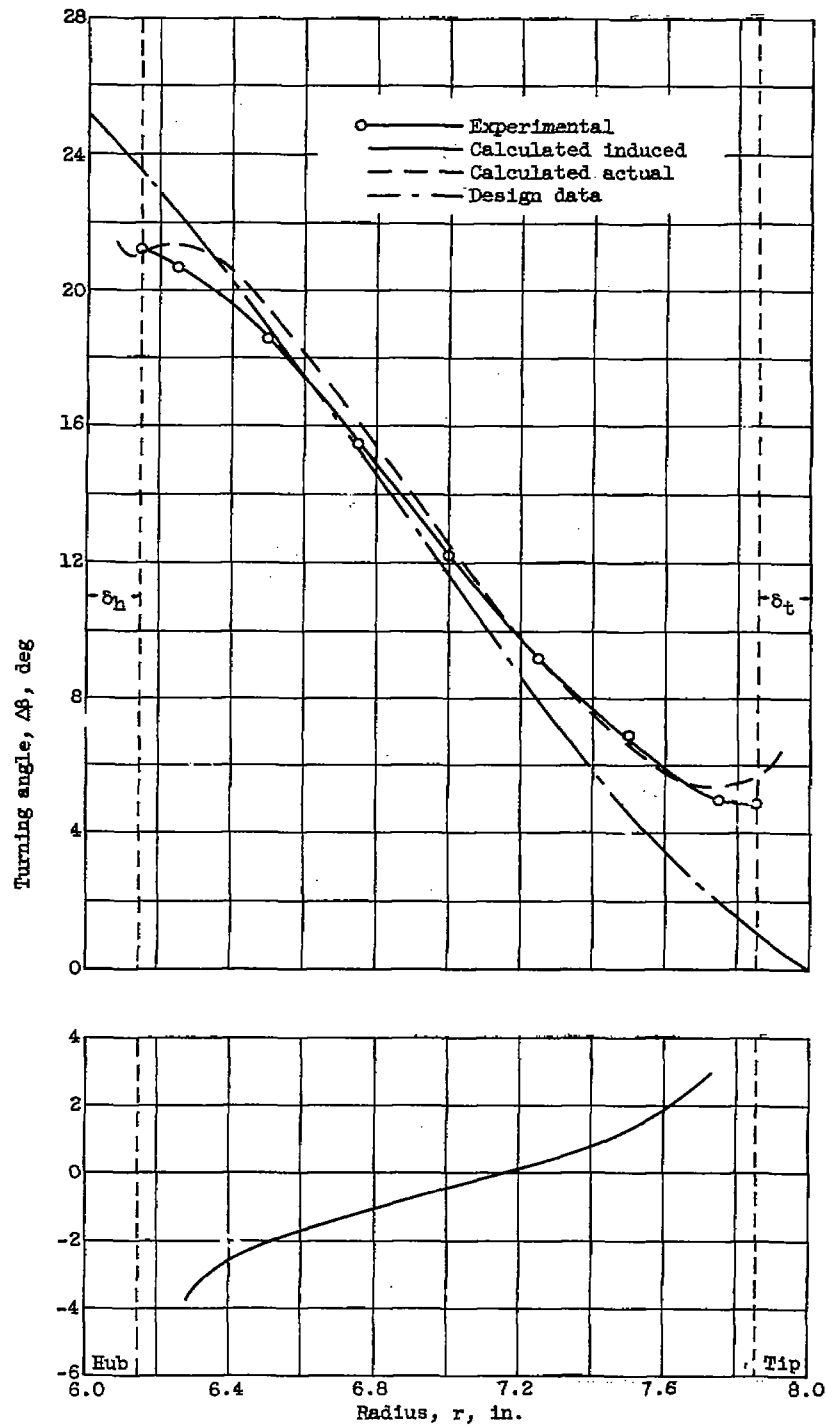


Figure 13. - Continued. Comparison of calculated and experimental turning angles of inlet guide vanes.

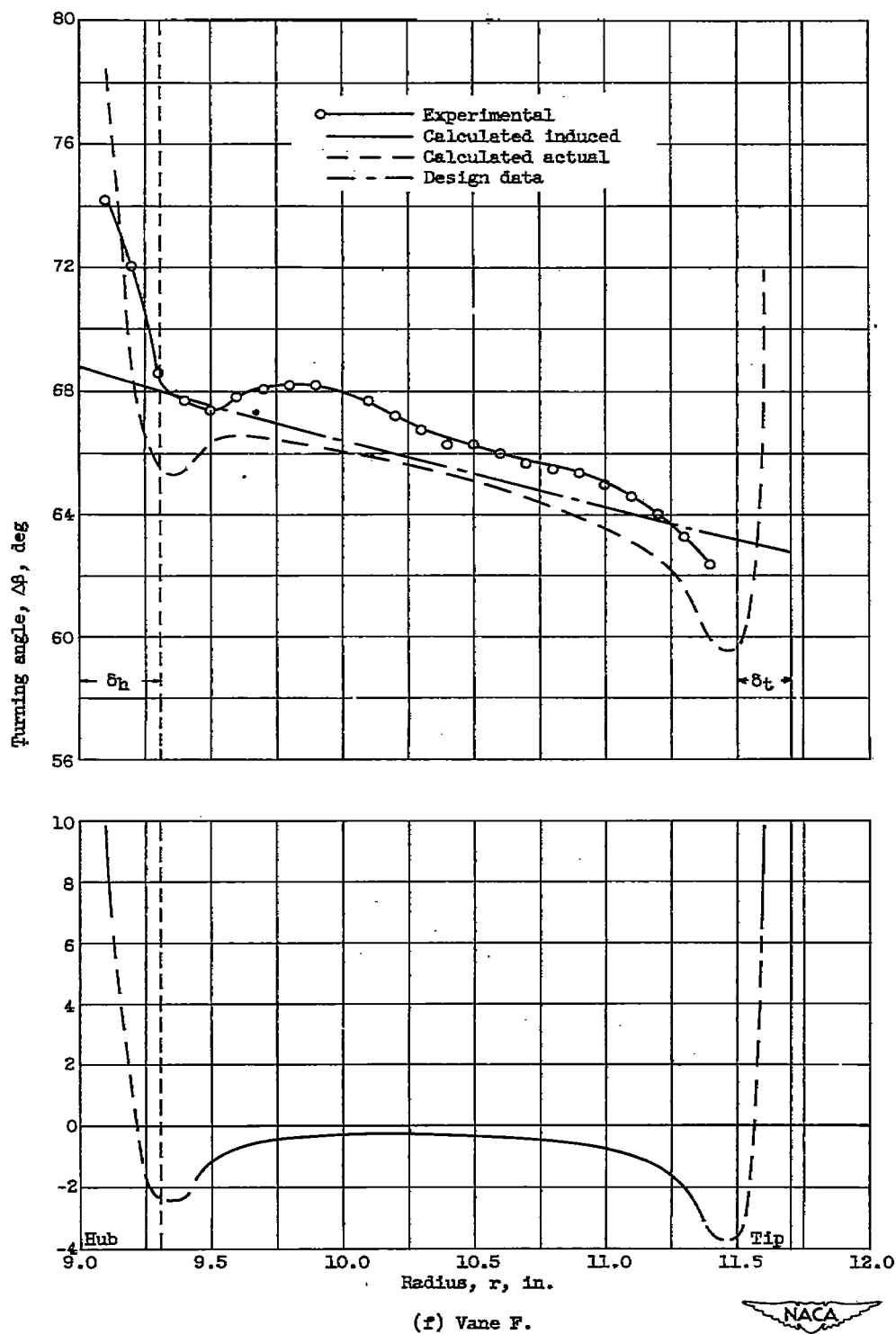


Figure 13. - Concluded. Comparison of calculated and experimental turning angles of inlet guide vanes.

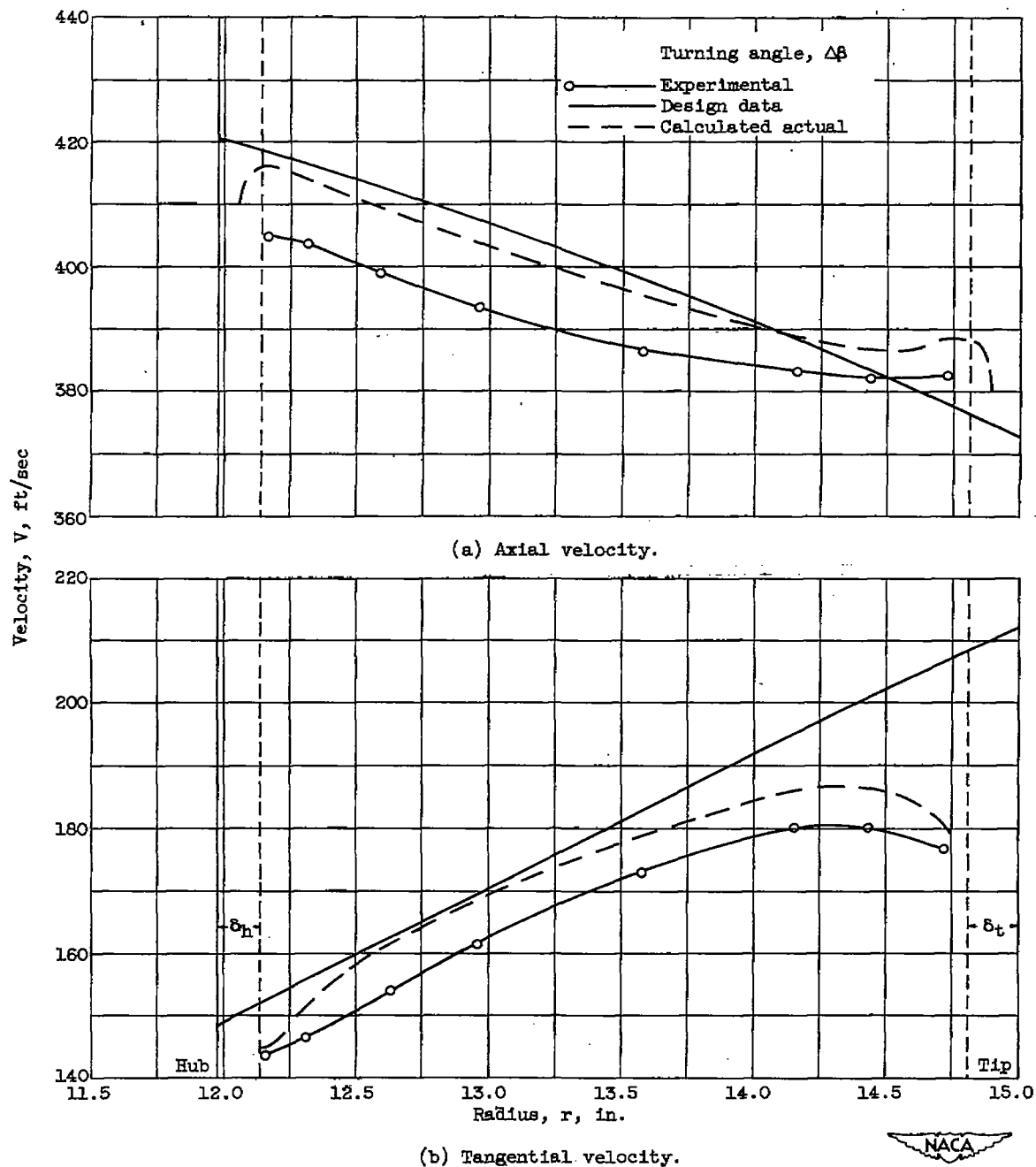
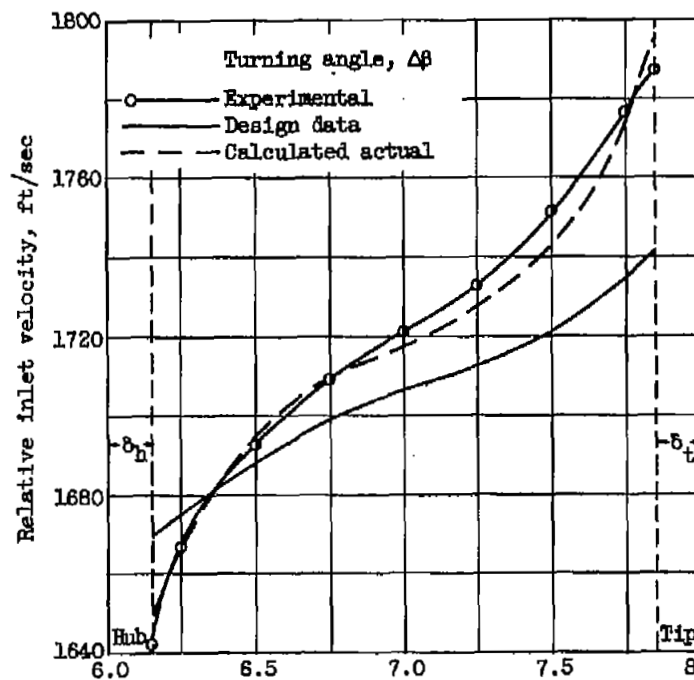
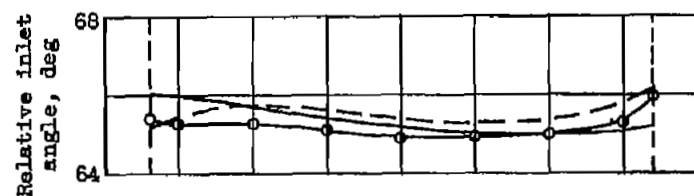
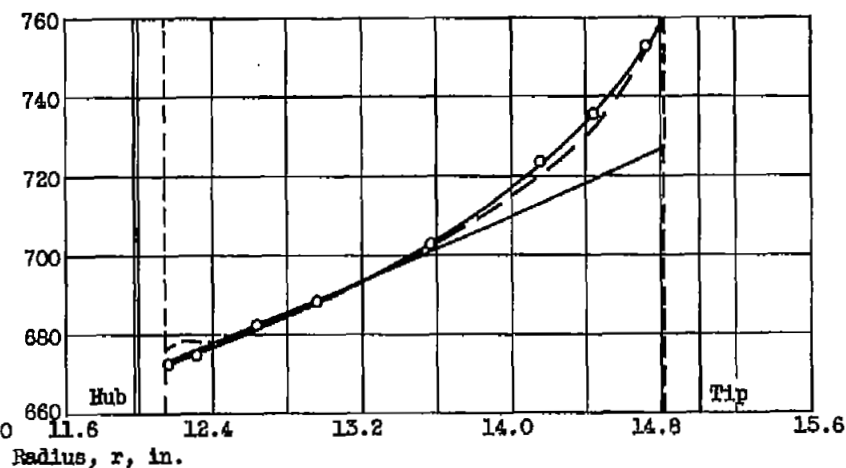
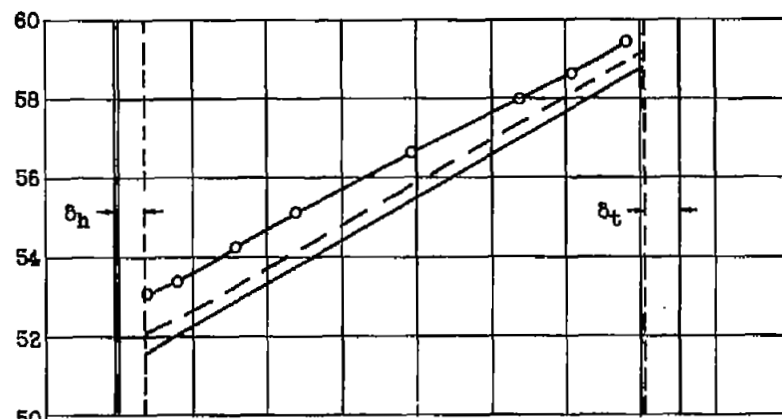


Figure 14. - Comparison of calculated and experimental velocities at outlet of vane C at design weight flow. Flow-area contraction ratio, 0.97.



(a) Vane E.



(b) Vane C.

Figure 15. - Comparison of calculated and experimental rotor relative inlet angle and relative inlet velocity at design tip speed for two types of compressor inlet guide vane. Flow-area contraction ratio, 0.97.

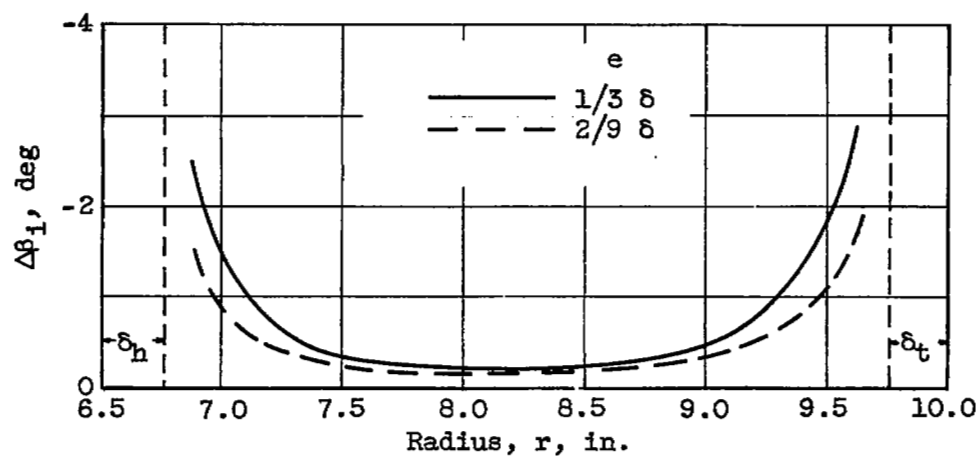


Figure 16. - Effect of location of boundary-layer vortex on calculated uncorrected induced turning angle for free-vortex inlet guide vane. M_1 , 0.4; $\Delta\beta_m$, 25° .

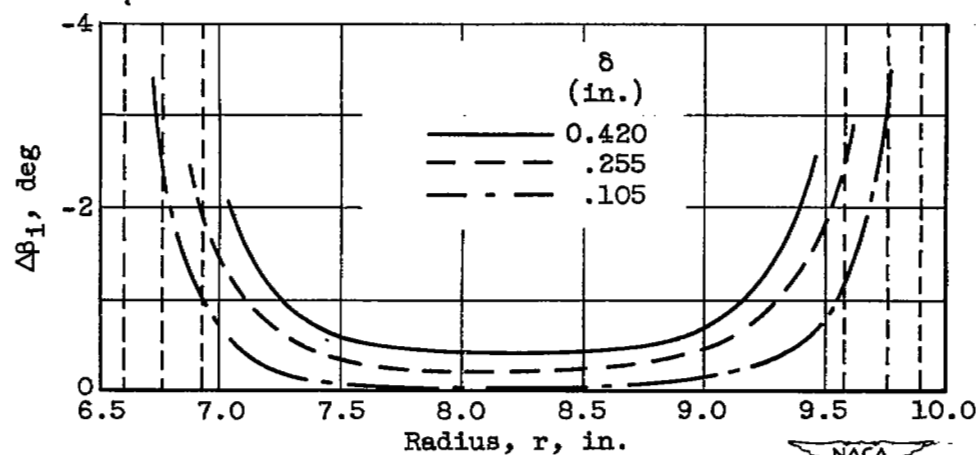


Figure 17. - Effect of boundary-layer thickness on calculated uncorrected induced turning angle for free-vortex inlet guide vane. M_1 , 0.4; $\Delta\beta_m$, 25° ; e , $1/3 \delta$.

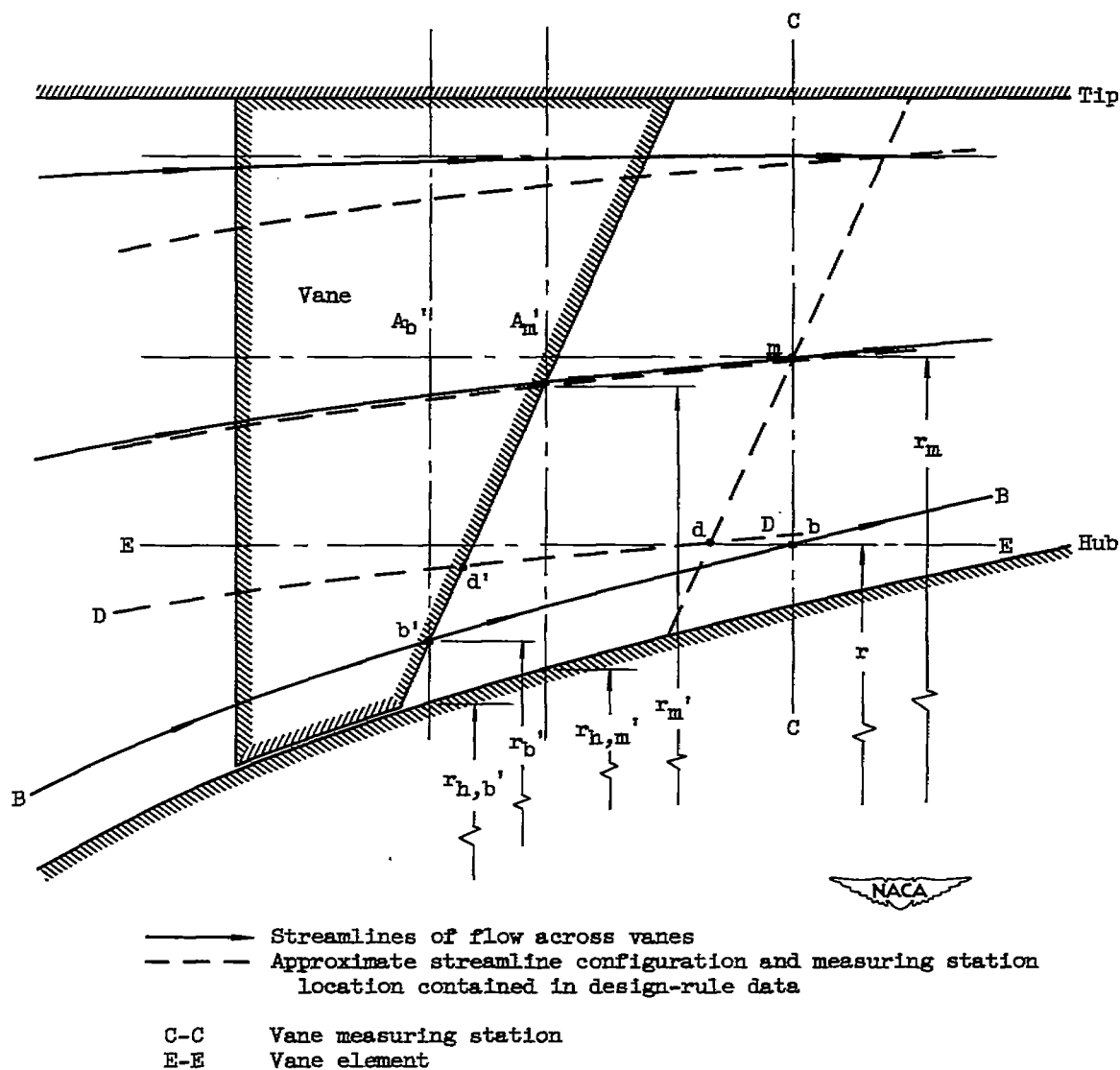


Figure 18. - Illustration of correction to design rule of reference 19 used for determination of radial variation of blade-element turning angle for circular-arc inlet guide vanes in convergent annuli.

NASA Technical Library



3 1176 01435 1408

